Annals of Nuclear Energy 196 (2024) 110235

Contents lists available at ScienceDirect

Annals of Nuclear Energy

journal homepage: www.elsevier.com/locate/anucene

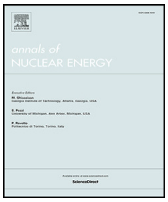

Development and verification of a one-dimensional collision probability based neutron transport code to model axially heterogeneous cylindrical vessels containing aqueous and organic plutonium nitrate

J.R. Daniels [*], M.M.R. Williams, M.D. Eaton

Nuclear Engineering Group, Department of Mechanical Engineering, City and Guilds Building (CAGB), Imperial College London, Exhibition Road, South Kensington Campus, London, SW7 2BX, United Kingdom

ARTICLE INFO

Keywords:
Collision probability
Neutron transport
Plutonium nitrate
Steady state
Development and verification

ABSTRACT

This paper presents the development and verification of a collision probability (CP) code, capable of modelling neutron transport in one-dimensional slabs and axially heterogeneous cylinders with varying radii. The CP code is used to model layered systems of aqueous and organic plutonium nitrate, as process criticality accidents are more likely to occur in these systems compared to dry systems. The use of the CP code is desired as it offers a computationally inexpensive method for calculating neutron transport when compared to higher fidelity codes such as MCNP. For slab geometries, the CP code can be used effectively, given they contain at least 0.7 g cm^{-2} plutonium. The approximation employed by the CP code to model heterogeneous cylinders overestimated the rate of radial neutron leakage such that vessels with radii of 30.0 cm could not reliably calculate reactivity to within 1 $ of MCNP. Increasing the radii to 40.0 cm improved the accuracy of the CP code to within 1 $ of MCNP for systems containing at least 2.75 kg plutonium. The error in the CP code increased when used to model cylindrical geometries with dished ends and complete vessels with dished ends, such that systems with large dished ends and low plutonium content should be avoided. As a simple, neutronics based model, the CP code could be used as part of rough order of magnitude calculations for criticality transients, where high levels of accuracy are not required, given that potential errors in results have been previously identified.

1. Introduction

Fissile liquid systems are present in the nuclear fuel cycle, most notably during solvent extraction processes, which includes the processing of ores, uranium purification, and waste reprocessing (e.g. during the PUREX process) (Crossland, 2012; Wilson, 1996; Zohuri, 2016). In the PUREX process, tri-*n*-butyl phosphate (TBP) is a commonly used solvent, with the solution being uranyl or plutonium nitrate (Irish and Reas, 1957). Fissile liquid systems can also be found in various experimental and research facilities (Crossland, 2012; McLaughlin et al., 2000; Wilson, 1996; Zohuri, 2016).

Process criticality accidents are more likely to occur in fissile solutions or liquid media (such as aqueous and organic plutonium nitrate) than in dry systems (McLaughlin, 2003). The primary hazards and dangers associated with accidental criticality include unexpected and unwanted radiation release, which can expose facility workers, the general public and the wider environment to ionising radiation (Crossland, 2012; Kimpland, 1993; Knief, 1985; Srinivasan et al., 1992), which can prove harmful to health, or even be fatal (Crossland, 2012; Knief, 1985). Additionally, the need for cleanup, on-site repair, increased healthcare and mitigation actions can result in significant economic costs (Bizet and Lévêque, 2017). Therefore, a comprehensive understanding of the physics of fissile liquid systems is important for the prevention and mitigation of nuclear criticality excursions (International Atomic Energy Agency, 2014).

To numerically determine the behaviour of nuclear systems, neutron transport codes can be employed, which use either Monte Carlo or deterministic methods (Hébert, 2020; Mohanakrishnan et al., 2021). Deterministic methods discretise the system across all phase-space variables: either finite difference, finite volume or finite element (FE) methods are used to discretise the spatial variables; the angular variable can be discretised using spherical harmonic (P_N) and discrete ordinates methods; the multigroup method is used to discretise the energy distribution; and explicit or implicit time-stepping method are used to discretise the temporal variable (Hébert, 2020; Mohanakrishnan et al., 2021; Stacey, 2007).

This paper presents the development and verification of a CP code to model vessels containing aqueous and organic plutonium nitrate.

---

[*] Corresponding author.
E-mail address: j.daniels15@imperial.ac.uk (J.R. Daniels).

https://doi.org/10.1016/j.anucene.2023.110235
Received 12 July 2023; Received in revised form 29 September 2023; Accepted 8 November 2023

Nomenclature

Acronyms

CP	Collision probability
MC	Monte Carlo
P0 TC	Isotropic scattering method with transport correction
P1	Linearly anisotropic scattering method
pcm	per cent mille

Latin Symbols

$\mathbf{r}$	Position vector, units of each component are [cm]
B^2	Radial geometric buckling [cm^{-2}]
D	Neutron diffusion coefficient [cm]
E	Energy [MeV]
G	Number of discrete energy groups [–]
h	thickness [cm]
k_{eff}	Effective multiplication factor [–]
$P_{i,j}$	Probability that a neutron born in cell j will experience its first collision in cell i [–]
R	Radius [cm]
R_A	Neutron absorption rate [cm^{-3} s^{-1} MeV^{-1}]
R_P	Neutron production rate [cm^{-3} s^{-1} MeV^{-1}]
S	Neutron source [neutrons cm^{-3} s^{-1} MeV^{-1}]
s	Distance between two points [cm]
V	Volume [cm^3]
z	z-coordinate [cm]
N	Order of spherical harmonic expansion [–]
[H]	Aqueous phase excess acid concentration [mol L^{-1}]
[Pu]	Aqueous phase plutonium concentration [g L^{-1}]

Greek Symbols

α	Volume fraction of aqueous phase in the mixed region [–]
χ	Prompt neutron energy spectrum [MeV^{-1}]
λ	Neutron mean free path [cm]
$\mathbf{\Omega}$	Solid angle [steradian]
ν	Average number of neutrons produced per fission [neutrons fission^{-1}]
ϕ	Scalar neutron flux [neutrons cm^{-2} s^{-1} MeV^{-1}]
ψ	Angular neutron flux [neutrons cm^{-2} s^{-1} MeV^{-1} steradian^{-1}]
ρ	Reactivity [\$]
Σ_a	Macroscopic neutron absorption cross section [cm^{-1}]
Σ_f	Macroscopic neutron fission cross section [cm^{-1}]
Σ_s	Macroscopic neutron scattering cross section [cm^{-1}]
Σ_t	Macroscopic neutron total cross section [cm^{-1}]
Σ_{tr}	Macroscopic neutron transport cross section [cm^{-1}]
τ	Neutron optical path [–]

Subscripts

g	Energy group index
i	Index of neutron collision cell
j	Index of neutron source cell
aqu	Aqueous region
dish	Dished end
mix	Mixed region
org	Organic region

Results from the CP code are verified by comparing them to MC code MCNP, with Serpent (also MC) being used to ensure the correct use and adequate results are obtained from MCNP. To compare the CP code to another deterministic method, FE and P_N based neutron transport research code EVENT will be utilised. Finally, to generate macroscopic neutron cross sections and provide a benchmark CP solution, lattice nuclear reactor physics code WIMS will be used.

As such, Section 2 of this paper describes a brief theory and description of the neutron transport codes deployed, with Section 3 detailing the development of the CP code. Section 4 highlights the need for suitable refinement of the deterministic codes' discretisations, and determines the discretisations used in Section 5, which details the verification of the CP code. Section 5 will detail the verification of the CP for geometries of increasing complexity, from one-dimensional (1D) slab geometry models to multidimensional models of complete vessels.

The motivation for developing and verifying a CP code is to determine whether this low-fidelity, computationally inexpensive method can model fissile liquid systems with a prescribed level of numerical accuracy. If so, it will be coupled to neutron kinetics and thermal-hydraulic feedback models in subsequent research, to determine the behaviour of criticality transients in layered fissile liquid systems. As such, understanding the deficiencies and inaccuracies in the CP models enables the understanding of modelling uncertainties in coupled point kinetics and thermal-hydraulic feedback models.

2. Computational modelling and simulation of steady-state nuclear criticality

2.1. The neutron transport equation

The steady-state neutron transport equation (NTE) describes the population of neutrons through a six-dimensional phase space of solution variables: position (x, y, z); energy (E); and angular direction ($\mathbf{\Omega}$):

$$\begin{aligned}&\mathbf{\Omega}\cdot\nabla\psi\left(\mathbf{r},\mathbf{\Omega},E\right)+\Sigma_t\left(\mathbf{r},\mathbf{\Omega},E\right)\psi\left(\mathbf{r},\mathbf{\Omega},E\right)=\\&\int_0^\infty dE'\int_{4\pi}d\mathbf{\Omega}'\,\Sigma_s\left(\mathbf{r},\mathbf{\Omega}\cdot\mathbf{\Omega}',E'\rightarrow E\right)\psi\left(\mathbf{r},\mathbf{\Omega}',E'\right)+S\left(\mathbf{r},\mathbf{\Omega},E\right),\end{aligned}\tag{1}$$

where, ψ is the angular neutron flux; Σ_t and Σ_s are the macroscopic total and scattering neutron cross sections respectively; and $S\left(\mathbf{r},\mathbf{\Omega},E\right)$ represents the neutron source (Cacuci, 2010; de Oliveira, 2001a; Ornstein and Uhlenbeck, 1937). The presented research is concerned only with the fission neutron source, which is assumed to be isotropic (Cacuci, 2010; de Oliveira, 2001a):

$$\begin{aligned}S\left(\mathbf{r},\mathbf{\Omega},E\right)&=\frac{1}{k_{\text{eff}}}S_{\text{fiss}}\left(\mathbf{r},E\right)=\frac{\chi(\mathbf{r},E)}{4\pi k_{\text{eff}}}\int_0^\infty dE'\int_{4\pi}d\mathbf{\Omega}'\nu(E')\Sigma_f\left(\mathbf{r},E'\right)\\&\quad\times\psi\left(\mathbf{r},\mathbf{\Omega}',E'\right).\end{aligned}\tag{2}$$

In these equations, k_{eff} is the effective multiplication factor and $\chi(\mathbf{r},E)$ is the probability density function describing the exit energy, E, of prompt neutrons produced by fission, and is assumed to be independent of the energy and direction of the incident neutrons causing fission. $\Sigma_f(\mathbf{r},E')$ is the macroscopic neutron fission cross section for neutrons of energy E'; $\nu(E')$ is the average number of neutrons produced by a fission induced by a neutron of energy E'.

To solve the steady-state NTE, the Monte Carlo (MC) method simulates individual particle histories from their production to their scattering, absorption and leakage from the system. Conversely, deterministic methods discretise the steady-state NTE in space, energy and angle using numerical discretisation methods.

2.2. Monte Carlo neutron transport codes

MCNP (Werner et al., 2018) and Serpent (Leppänen et al., 2015) are two MC codes which are capable of continuous-energy, three-dimensional (3D) analysis of nuclear criticality, and have been widely verified and validated (Leppänen et al., 2015; Werner et al., 2018). This paper presents results from both codes: comparing MCNP and Serpent ensures their correct use and confidence in their outputs. Throughout this paper, results from MCNP and Serpent will be given with their statistical uncertainty equal to one standard deviation.

2.3. The deterministic neutron transport code EVENT

EVENT is an academic research code which solves the multigroup, second-order even-parity (EP) form of the NTE (Vladimirov, 1963), assuming that neutron scattering is rotationally symmetric and that the neutron fission source is isotropic. It can model multidimensional, curvilinear geometries due to the use of a geometry conforming, finite element (FE) spatial discretisation (de Oliveira, 1987, 2001a,b). The anisotropy in the angular neutron flux and the scattering are modelled by expanding the angular dependence of the angular neutron flux using spherical harmonic (P_N) basis functions, and expanding the macroscopic double differential neutron scattering cross section using Legendre polynomials basis functions (de Oliveira, 1987, 2001a).

2.4. The WIMS nuclear reactor lattice physics code

WIMS is a modular nuclear reactor lattice physics code used to perform neutron transport simulations for thermal spectrum nuclear reactors such as light water reactors (LWRs), advanced gas cooled reactors (AGRs), and high temperature gas cooled reactors (HTGRs) (Askew et al., 1966; Lindley et al., 2015, 2017).

In the presented research, the starting module HEAD is used, which loads nuclear data, reads the geometry and material specifications, and corrects the microscopic cross sections to account for energy and spatial resonance self shielding phenomena (using equivalence modelling, with a resonance range from 4 eV to 183 keV) and Doppler temperature broadening (Askew et al., 1966; Lindley et al., 2015, 2017).

If this equivalence treatment is inadequate, HEAD can be coupled with PRES-X-RES, where ‘X’ is a suitable solution module (the presented research uses THESEUS, a collision probability module) (Carlvik, 1966; Jonsson, 1963; Powney and Newton, 2004; Roth, 1980, 1983, 1985).

PRES fits subgroup cross sections to the library resonance integrals; THESEUS calculates the collision probabilities for these cross sections (Carlvik, 1966; Roth, 1985); RES uses these probabilities to calculate subgroup fluxes and weights for each WIMS library resonance group (Roth, 1974, 1983). The output from RES is a new set of broad-group cross sections, calculated from the subgroup fluxes and resonance group weights (Roth, 1974, 1983).

THESEUS and PIP (a collision probability solution module) are used to solve the multigroup NTE (Askew and Roth, 1982; Carlvik, 1966; Jonsson, 1963; Roth, 1985), with the CONDENSE module used to achieve the desired energy group discretisations (Gubbins and Roth, 1980).

2.5. The transport neutron cross-section

Generally, the double differential neutron scattering macroscopic cross section, $\Sigma_s(E \to E', \mu)$, is calculated by using a Legendre expansion in terms of μ, the deviation cosine, as in Eq. (3) (Bell et al., 1967; Chiba, 2004; Hébert, 2020):

$$\Sigma_s(E \to E', \mu) = \sum_{l=0}^{L} \frac{2l+1}{2} \Sigma_{s,l}(E \to E') P_l(\mu), \tag{3}$$

where $\Sigma_{s,l}(E \to E')$ is the lth order Legendre component of $\Sigma_s(E \to E', \mu)$:

$$\Sigma_{s,l}(E \to E') = \int_{-1}^{1} d\mu \ \Sigma_s(E \to E', \mu) P_l(\mu) \tag{4}$$

and $P_l(\mu)$ is the lth order Legendre polynomial.

Isotropic scattering and linearly anisotropic scattering correspond to L equal to 0 and 1, respectively (Bell et al., 1967; Hébert, 2020). Although assuming linear scattering anisotropy is generally acceptable in reactor physics, assuming isotropic scattering is not. Therefore, to account for scattering anisotropy without the need for the Legendre expansion, a transport correction needs to be applied (Bell et al., 1967; Hébert, 2020; Petkov and Takeda, 1998; Ushio et al., 2003; Yamamoto et al., 2008).

One example of a transport correction is the use of transport neutron cross sections: linearly anisotropic (P1) cross sections are approximated by modifying the isotropic (P0) cross sections, which are otherwise used explicitly (Ushio et al., 2003; Yamamoto et al., 2008).

There are various methods to calculate transport neutron cross sections (Chiba, 2004; Honeck, 1964; Yamamoto et al., 2008). For example, the in-scatter approximation calculates the macroscopic transport neutron cross section, $\Sigma_{tr,g}$, using

$$\Sigma_{tr,g} = \Sigma_{t,g} - \frac{\sum_{g'} \Sigma_{s,1,g' \to g} \psi_{1,g'}}{\psi_{1,g}}, \tag{5}$$

where $\psi_{1,g}$ is the P1 component of the angular flux (equivalent to the neutron current) (Bell et al., 1967; Chiba, 2004; Yamamoto et al., 2008).

The out-scatter approximation is a simplification of the in-scatter approximation (Yamamoto et al., 2008), where it is assumed that

$$\sum_{g'} \Sigma_{s,1,g' \to g} \psi_{1,g'} \approx \sum_{g'} \Sigma_{s,1,g' \to g} \psi_{1,g}, \tag{6}$$

meaning $\Sigma_{tr,g}$ can be calculated using (Bell et al., 1967; Honeck, 1964; Ushio et al., 2003; Yamamoto et al., 2008):

$$\Sigma_{tr,g} = \Sigma_{t,g} - \sum_{g'} \Sigma_{s,1,g \to g'}. \tag{7}$$

Generally, the in- and out-scatter approximations agree well for neutron energies < 1 keV; for neutron energies ≥ 1 keV, the in-scatter approximation is used (Petkov and Takeda, 1998; Yamamoto et al., 2008).

WIMS calculates $\Sigma_{tr,g}$ using the out-scatter approximation (Eq. (7)) for neutrons with energy < 4 eV. For neutrons with energy ≥ 4 eV, resonance phenomena needs to be accounted for (Coulson, 1999), and the in-scatter approximation (Eq. (5)) is used (Dean, 1993; Lindley et al., 2015; Powney and Newton, 2004; Roth, 1980, 1983). Conversely, Serpent uses the in-scatter approximation using Eq. (5) for all neutron energies (Leppänen et al., 2016).

2.6. Normalisation of results

In order to directly compare the various codes' numerical results, they need to be identically normalised. The normalisation used by MCNP (Werner et al., 2018), the CP code and EVENT is

$$\int_E dE \int_V d^3r \ \nu\Sigma_f(\mathbf{r}, E)\phi(\mathbf{r}, E) = k_{\text{eff}}, \tag{8}$$

which will be used as standard in the presented research. WIMS results are normalised using

$$\int_E dE \int_V d^3r \ \nu\Sigma_f(\mathbf{r}, E)\phi(\mathbf{r}, E) = C_1, \tag{9}$$

where C_1 is a user-defined constant (Lindley et al., 2015, 2017). To yield the standard normalisation, C_1 is set equal to the k_{eff} from that

WIMS simulation. Similarly, the normalisation of Serpent results can be described using

$$\int_E dE \int_V d^3r \; \nu\Sigma_f(\mathbf{r},E)\phi(\mathbf{r},E) = \frac{C_2}{V}, \tag{10}$$

where C_2 is user defined (set to k_{eff} in the presented research) and the volume term, V, can be removed during post-processing.

2.7. Comparison of numerical results

To determine their effectiveness, results produced from each of the codes will be compared to those produced using MCNP. When comparing k_{eff} values, the following definition will be used:

$$\Delta k_{\mathrm{eff,A}}\ (\mathrm{pcm}) \ = \frac{k_{\mathrm{A}} - k_{\mathrm{MCNP}}}{k_{\mathrm{MCNP}}} \times 10^5, \tag{11}$$

where k_{A} is the k_{eff} produced from code 'A', and k_{MCNP} is the k_{eff} predicted by MCNP. The same relation will be used for infinite multiplication factor (k_∞) comparisons.

When comparing reactivity (ρ), the absolute difference between MCNP and the other codes investigated will be used, i.e $\Delta\rho_{\mathrm{A}}$ (\$) $= \rho_{\mathrm{A}} - \rho_{\mathrm{MCNP}}$.

When comparing other results (reaction rates, fluxes, etc.), the difference between MCNP and the other codes investigated will be expressed as a percentage, i.e.

$$\Delta X_{\mathrm{A}}\ (\%) \ = \frac{X_{\mathrm{A}} - X_{\mathrm{MCNP}}}{X_{\mathrm{MCNP}}} \times 10^2, \tag{12}$$

where X is the result being compared (reaction rate, flux, etc.) and 'A' is the code being investigated.

2.7.1. Prescribed levels of accuracy

As described in Section 1, the motivation of the presented research is to determine whether the developed CP code can model fissile liquid systems accurately enough to assist in the determination of the behaviour of criticality transients in layered fissile liquid systems, an area of subsequent research.

The transient criticality analysis will be based on the energy balance of coupled point kinetics and thermal-hydraulic feedback models, to provide order of magnitude calculations to assist in safety and risk assessment analysis. Thus, in the coupled neutronics models, large degrees of accuracy are not required, and quick methods of reactivity calculation are desired.

As such, in the presented research, calculated values of reactivity should be within 1 \$ of MCNP, and values of reaction rates and scalar neutron fluxes should be within 5% of MCNP.

2.8. Nuclear data libraries

The ENDF (Evaluated Nuclear Data File) libraries, have been chosen for this study. The most recent major release has been version ENDF/B-VIII.0 (Brown et al., 2018; Conlin et al., 2013), which is recommended for use in all MC transport calculations (Conlin et al., 2013). Though this data exists in formats useable by MCNP (Conlin et al., 2013) and WIMS, it is not yet readily available in a format that can be used by Serpent. As such, ENDF/B-VII.1 (Chadwick et al., 2011; Conlin et al., 2013), the second most recent release, will be used in this work. The notable relevant difference between ENDF/B-VII.1 and ENDF/B-VIII.0 is the update to average resonance and prompt neutrons produced per fission of ^{239}Pu: ENDF/B-VII.1 is known to overpredict the k_{eff} of thermal plutonium solutions (Brown et al., 2018; Chadwick et al., 2011). Thus, k_{eff} values produced in this work are likely to be overestimates of the true value.

3. Development of the collision probability code

Collision probability (CP) methods are based on the integral, steady-state form of the NTE (Peierls, 1939),thorough descriptions of which are well documented (e.g. Cacuci, 2010; Duderstadt and Martin, 1979; Hébert, 2020; Lefvert, 1979), and, assuming isotropic fission neutron source, is defined as

$$\psi(\mathbf{r},E,\mathbf{\Omega}) = \int_0^\infty ds\; e^{-\tau(s,E)}Q(\mathbf{r}-s\mathbf{\Omega},E,\mathbf{\Omega}), \tag{13}$$

$$Q(\mathbf{r},E,\mathbf{\Omega}) = \int_0^\infty dE' \int_{4\pi} d\mathbf{\Omega}'\,\Sigma_s\left(\mathbf{r},\mathbf{\Omega}\cdot\mathbf{\Omega}',E'\to E\right)\psi\left(\mathbf{r},\mathbf{\Omega}',E'\right) + \frac{1}{k_{\mathrm{eff}}}S_{\mathrm{fiss}}(\mathbf{r},E), \tag{14}$$

where τ is the neutron optical path (Cacuci, 2010; Duderstadt and Martin, 1979; Hébert, 2020; Lefvert, 1979):

$$\tau(s,E) = \int_0^s ds'\,\Sigma_t(\mathbf{r}-s'\mathbf{\Omega},E). \tag{15}$$

By assuming isotropic scattering and source, and by integrating over the solid angles, the steady-state NTE can be discretised in space and energy, yielding a matrix of collision probabilities, where an element $P_{i,j}$ is the probability that a neutron born in cell j will experience its first collision in cell i (Cacuci, 2010; Duderstadt and Martin, 1979; Hébert, 2020). For a multi-group system, the collision probability equations are:

$$\phi_{i,g} = \sum_j Q_{j,g}\;P_{i,j,g}\;\Sigma_{t,j,g}^{-1}, \tag{16}$$

where

$$Q_{j,g} = \sum_{g'=1}^{G}\Sigma_{s,j,g\leftarrow g'}\phi_{j,g'} + \frac{1}{k_{\mathrm{eff}}}\chi_{j,g}\sum_{g'=1}^{G}\nu\Sigma_{f,j,g'}\phi_{j,g'} \tag{17}$$

and

$$P_{i,j}\Sigma_{t,j}^{-1} = \frac{1}{4\pi V_i}\int_{V_i} d^3r' \int_{V_j} d^3r\;\frac{e^{-\tau(s)}}{s^2}. \tag{18}$$

Here, V is the volume, d^3r and d^3r' are elemental volumes. The form of the optical path and integrals in Eq. (18) will vary depending on the system's geometry (Hébert, 2020).

Whilst the CP method can handle complex geometries, the coupling of every cell to every other cell in the system means the computation time increases proportional to I^2G, where I is the number of cells in the system, and G the number of neutron energy groups (Cacuci, 2010; Hébert, 2020). Thus, it is desirable to limit solving the CP equations to systems with few cells. In the presented research, this will be achieved by limiting system geometries to one dimension.

3.1. The one-dimensional slab model

In the presented research, a code capable of solving the CP equations for one-dimensional (1D) slab geometries, for any I and G, was developed. Linearly anisotropic scattering can be accounted for in the code by the use of transport corrected neutron cross sections (as described in Section 2.5).

An example slab geometry in z is shown in Fig. 1, which consists of three regions, with heights H_1, H_2, and H_3 respectively. The regions are discretised into multiple cells, with the exact number of cells per region depending on the level of mesh refinement used.

3.2. A radially homogeneous and axially heterogeneous cylindrical model

To approximate a cylinder that is radially homogeneous and axially heterogeneous, the CP code assumes a 1D slab geometry, and uses an approximation based on neutron diffusion theory to account for radial leakage of neutrons.

Neutron diffusion theory is well detailed in the literature (see Lee, 2020; Oka, 2014; Stacey, 2007). The approximation uses the neutron diffusion coefficient, D, defined in Eq. (19), and the radial geometric buckling, B^2, defined in Eq. (20) for a cylinder in a vacuum, where Σ_{tr}

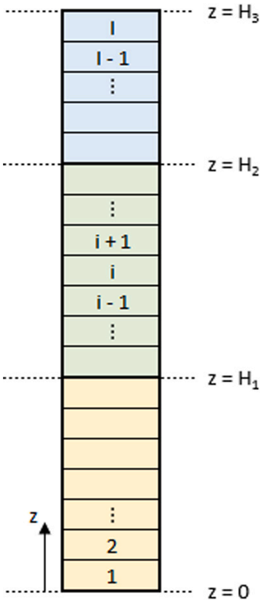

Fig. 1. The discretisation used in the CP code, with each region displayed in a different colour, and regions and cells numbered from bottom to top.

is the macroscopic neutron transport cross section (Lee, 2020; Stacey, 2007), $2D$ is the neutron flux extrapolation distance, and R is the vessel radius (Knief, 1985; Stacey, 2007).

An adjustment is made to the material's macroscopic neutron absorption cross section, Σ_a, so that the radial leakage of neutrons from the system, DB^2, is accounted for by artificially increasing the rate of absorption in the system. This is demonstrated in Eq. (21).

$$D_g = \frac{1}{3\Sigma_{tr,g}} \tag{19}$$

$$B_g^2 = \left(\frac{2.405}{R+2D_g}\right)^2 \tag{20}$$

$$\Sigma_{a,g,\text{corrected}} = \Sigma_{a,g} + D_g B_g^2 \tag{21}$$

This correction is done for every material and every energy group, and it is assumed that the rate of axial neutron leakage is adequately predicted by the 1D slab model.

3.3. Accounting for dished ends

In industrial applications and research facilities, vessels containing aqueous and organic plutonium nitrate are not limited to flat-bottomed cylinders, but are often cylindrical in shape with dished ends.

To enable the modelling of dished ends in the CP code, the properties D and B^2 can be made height dependent by making R height dependent. Taking i to be the index of the ith cell of the discretised system, Eqs. (19)–(21) can be rewritten as

$$D_{i,g} = \frac{1}{3\Sigma_{tr,i,g}}, \tag{22}$$

$$B_{i,g}^2 = \left(\frac{2.405}{R_i+2D_{i,g}}\right)^2, \tag{23}$$

$$\Sigma_{a,i,g,\text{corrected}} = \Sigma_{a,i,g} + D_{i,g} B_{i,g}^2. \tag{24}$$

Thus, it can be seen that each cell of the discretised system can have a different radius associated with it, and therefore different values of $D_{i,g}$ and $B_{i,g}^2$ and $\Sigma_{a,i,g,\text{corrected}}$ when compared to neighbouring cells consisting of the same material.

3.4. Justification of the buckling approximation

As shown in Williams (1971), for a homogeneous system, the mono-energetic integral form of the NTE (originally defined in Eq. (13)) can be written as

$$\phi(\mathbf{r}) = \left(\frac{1}{k_{\text{eff}}}\nu\Sigma_f + \Sigma_s\right)\int_V d\mathbf{r}'\ \phi(\mathbf{r}')\frac{e^{\Sigma_t|\mathbf{r}-\mathbf{r}'|}}{4\pi(\mathbf{r}-\mathbf{r}')^2} \tag{25}$$

where isotropic scattering and fission source have been assumed, and no significant extraneous source is present. By assuming a solution of the form

$$\phi(\mathbf{r}) = \phi(r,z) = \phi(B,z)e^{i\mathbf{B}\cdot\mathbf{r}}, \tag{26}$$

where $d\mathbf{r} = dzrdrd\varphi$ and $\mathbf{B}\cdot\mathbf{r} = Br\cos\varphi$, and integrating over $r(0,\infty)$ and $\varphi(0,2\pi)$, Eq. (25) can be written as (Williams, 1971):

$$\phi(B,z) = \left(\frac{1}{k_{\text{eff}}}\nu\Sigma_f + \Sigma_s\right)\int_0^H dz'\ \phi(B,z')K(B;|z-z'|). \tag{27}$$

Here, B^2 is the radial buckling, i.e. $B^2 = (2.405/R)^2$, and $K(B;|z-z'|)$ is a kernel of the form

$$K(B;|z-z'|) = \frac{1}{2}\int_0^1 d\mu\ \frac{\Sigma_t}{\mu\sqrt{\Sigma_t^2+\mu^2B^2}}\exp\left(-\frac{|z-z'|}{\mu}\sqrt{\Sigma_t^2+\mu^2B^2}\right). \tag{28}$$

Assuming the scalar neutron flux is constant throughout, k_{eff} can be approximated by integrating Eq. (27) over the domain, yielding

$$\begin{aligned}\frac{\Sigma_t}{\frac{1}{k_{\text{eff}}}\nu\Sigma_f+\Sigma_s} &= \frac{\tan^{-1}\overline{B}}{\overline{B}} - \frac{1}{H\Sigma_t\overline{B}^2}\left(1-\frac{1}{\sqrt{1+\overline{B}^2}}\right)\\ &+ \frac{1}{H\Sigma_t}\int_0^1 d\mu\ \frac{\mu\exp\left(-\frac{H\Sigma_t}{\mu}\sqrt{1+\mu^2\overline{B}^2}\right)}{\left(1+\mu^2\overline{B}^2\right)^{3/2}},\end{aligned} \tag{29}$$

where $\overline{B} = B/\Sigma_t$. If there is no transverse leakage, $B = 0$, and Eq. (27) instead becomes

$$\begin{aligned}\frac{\Sigma_t}{\frac{1}{k_{\text{eff}}}\nu\Sigma_f+\Sigma_s} &= 1-\frac{1}{2H\Sigma_t}+\frac{1}{H\Sigma_t}\int_0^1 d\mu\ \mu\exp\left(-\frac{H\Sigma_t}{\mu}\right)\\ &= 1-\frac{1}{2H\Sigma_t}+\frac{1}{H\Sigma_t}E_3(H\Sigma_t).\end{aligned} \tag{30}$$

The proposed method to model an axially heterogeneous cylinder using a slab in the CP code is to modify the neutron absorption cross sections used by the code, as described in Section 3.2. In this mono-energetic example, Eq. (21) is rewritten as $\Sigma_a = \Sigma_a + DB^2$. As $\Sigma_t = \Sigma_a + \Sigma_s$, Σ_t can also be re-written as $\Sigma_t = \Sigma_t + DB^2$. Inserting this modification into Eq. (30) yields

$$\frac{\Sigma_t+DB^2}{\frac{1}{k_{\text{eff}}}\nu\Sigma_f+\Sigma_s} = 1-\frac{1}{2H\left(\Sigma_t+DB^2\right)}+\frac{1}{H\left(\Sigma_t+DB^2\right)}E_3\left(H\left(\Sigma_t+DB^2\right)\right). \tag{31}$$

To demonstrate the effectiveness of the above approximation, k_{eff} values obtained from Eq. (31) were compared to those from Eq. (29), for various domain radii, R. The parameters used in the provided example are given in Table 1, where λ is the neutron mean free path.

The resulting k_{eff} variations with domain radius are shown in Fig. 2(a). As expected, as the domain radius increases, so does the k_{eff} of the system, reaching a plateau at larger radii (in this case when $R/\lambda > 50$). It is seen that for small radii relative to the neutron mean free path, the approximate solution performs poorly when compared to the analytic solution. Fig. 2(b) shows that, for $R/\lambda > 8$, Δk_{eff} varies proportional to $(R/\lambda)^{-2}$. As such, the performance of the approximation improves proportional to $(R/\lambda)^2$, for $R/\lambda > 8$. In this

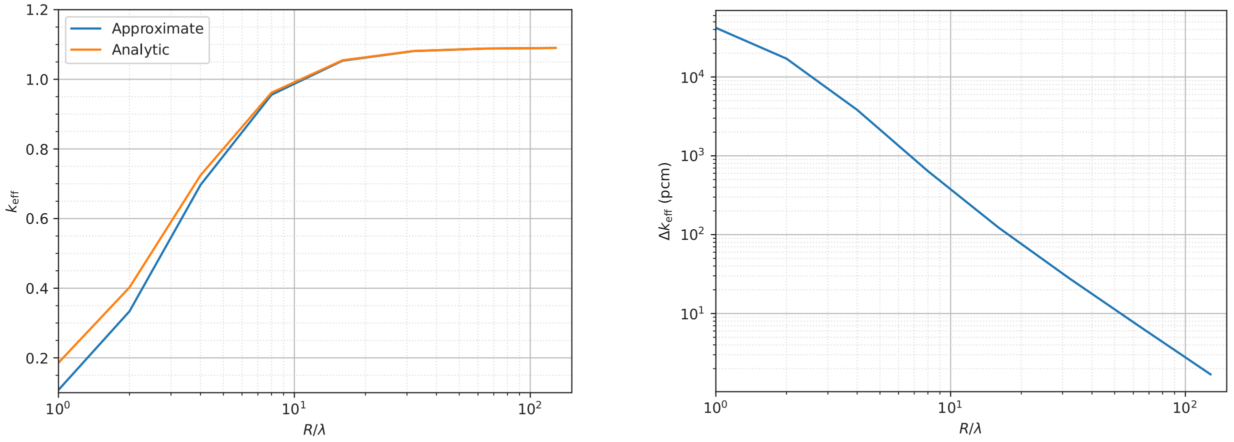

(a) The k_{eff} values from both methods.

(b) The difference in k_{eff} between the two methods.

Fig. 2. The k_{eff} values calculated using Eqs. (29) ('analytic') and (31) ('approximate'), and their relative differences, as functions of R/λ.

Table 1
Data and expressions used to demonstrate the error in the proposed buckling approximation.

Parameter	Unit	Value or Expression
H	cm	5
Σ_t	cm^{-1}	1.00
Σ_s	cm^{-1}	0.90
Σ_a	cm^{-1}	0.10
$\nu\Sigma_f$	cm^{-1}	0.23
B^2	cm^{-2}	$(2.405/R)^2$
$\overline{B}$	–	B/Σ_t
λ	cm	$1/\Sigma_t$

Table 2
Macroscopic neutron cross sections, and the corresponding R/λ, for an example set of nuclear data used in this work.

Group	Energy range (eV)	Σ_t (cm^{-1})	R/λ
1	(6.7–19.6) × 10^6	∼0.1	∼3
10	(6.8–14.3) × 10^2	∼0.6	∼17
20	(1.6–1.9) × 10^0	∼0.7	∼21
30	(0.0–1.3) × 10^{-1}	∼2	∼65

case, the difference between the analytic and approximate values for k_{eff} decreases to 28.00 pcm when $R = 32\lambda$. Thus, it can be concluded that the approximation developed here is sufficient for large domain radii relative to the neutron mean free path.

The cross sections used in this work vary considerably with energy. For the 30-group energy structure (detailed in Table B.16), a selection of approximate, transport-corrected values for Σ_t, along with the corresponding R/λ, for $R = 30.5$ cm, are given in Table 2. It can be seen that, as energy increases, Σ_t decreases; as such, R/λ increases. Notably, for energies above 14.3×10^2 eV, R/λ decreases below 17. For the example above, Fig. 2(b) indicates that R/λ decreasing much beyond 20 will induce errors of over 100 pcm. Thus, it is expected that the suitability of the proposed approximation will vary depending on the energy of the system being considered, in addition to the system's radius at a given height.

4. Refinement of deterministic codes

As the CP code, WIMS and EVENT are deterministic codes, they use discrete forms of the NTE. As such, refinement of the discretisations in space and energy is needed to obtain accurate results. This section presents an investigation into the levels of refinement needed for the three deterministic codes to be sufficiently accurate.

Table 3
The discretisations used in the refinement study.

Variable	Symbol	Discretisation values					Unit
Radial mesh spacing	Δr	6.1	3.05	1.525	0.61	0.305	cm
Axial mesh spacing	Δz	1	0.5	0.2	0.1	0.05	cm
No. energy groups	G	2	8	20	30	–	–
P_N expansion order	N	3	5	7	9	11	–

Two models are presented, a slab and an axially heterogeneous cylinder. Both models have vacuum boundary conditions and consist of three regions: $0.0 \leq z \leq 10.0$ cm, $10.0 \leq z \leq 15.0$ cm and $15.0 \leq z \leq 24.0$ cm. These regions consist of aqueous material, mixture A, and organic material respectively, with material compositions and densities detailed in Tables A.10–A.12. The discretisations used in the presented study are presented in Table 3, with the energy group discretisations detailed in Appendix B.

Fig. 3 shows how refining the discretisations of the slab and cylindrical models affects the value of k_{eff} calculated by the deterministic neutron transport codes.

The top-left graph of Fig. 3 demonstrates that decreasing Δz increases k_{eff}. For the slab geometry, k_{eff} converges to 1.030 for EVENT P0 TC, CP and WIMS calculations, and to 1.028 for EVENT P1 calculations. For both geometries, results from specific codes converge at the same rate. Results from the EVENT simulations appear to have converged with a Δz as high as 0.5 cm (corresponding to 48 axial mesh cells), which is due to the code's second order accuracy in the spatial domain. Being only first order accurate in space, the WIMS and CP codes take longer to converge; both need a Δz as low as 0.1 cm, corresponding to 240 axial cells in the system, to reach convergence.

The top-right graph of Fig. 3 shows how the number of energy groups affects the k_{eff} results. Again, for a specific code, the pattern of convergence is the same for both slab and cylindrical geometries. For all codes, the results are approaching convergence, though there is still some variation in the results when increasing from 20 to 30 energy groups. The EVENT P1 simulations are seen to vary considerably when increasing from 2 to 8 energy groups: for the slab geometry, k_{eff} drops from 1.07528 to 1.03236. The k_{eff} values from the three other deterministic codes all increase with increasing number of energy groups.

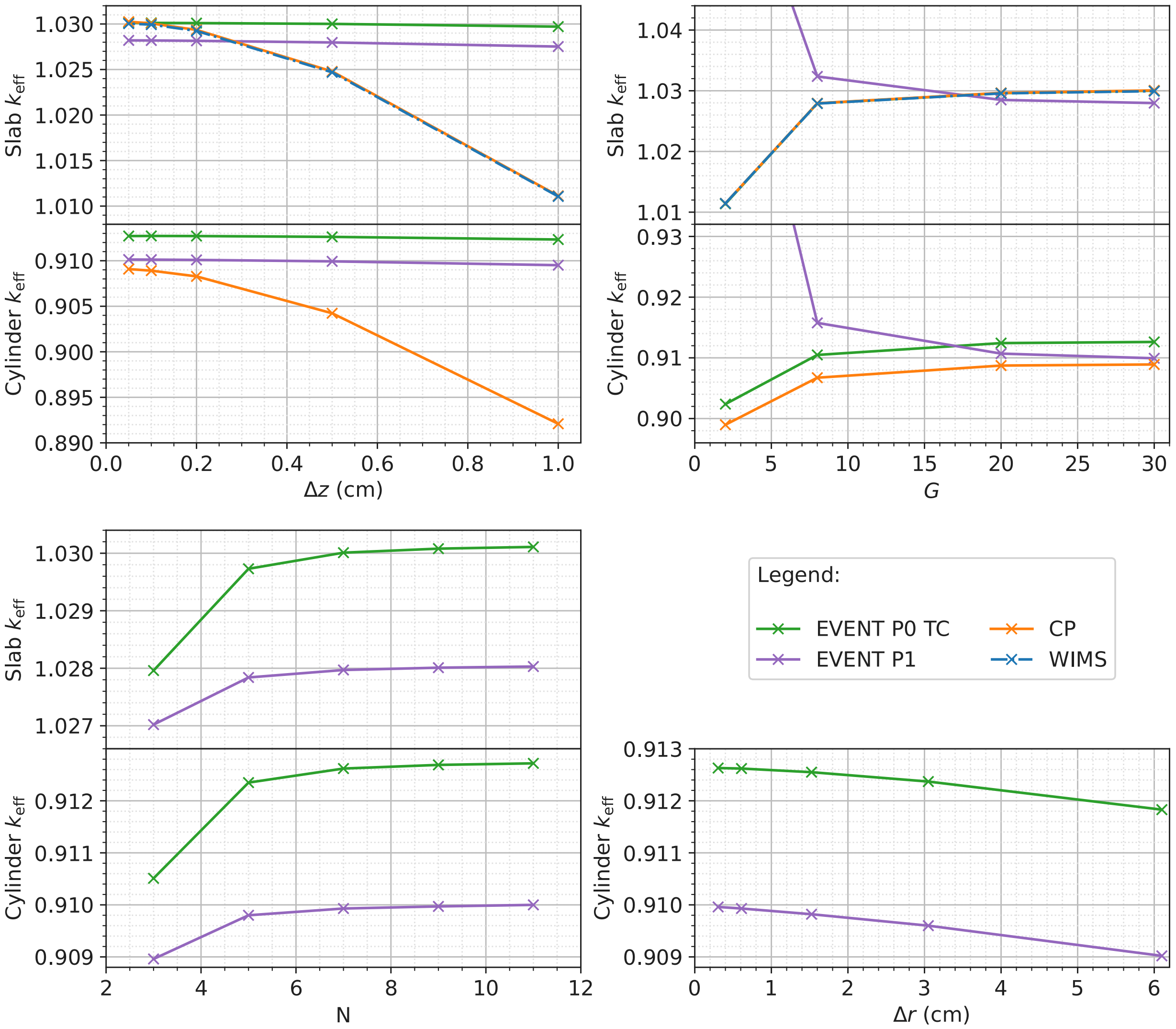

Fig. 3. Variation in k_{eff} with refinement of the phase-space variables. Unless being varied, EVENT simulations used $\Delta z = 0.5$ cm, $G = 30$, N = 7 and $\Delta r = 0.61$ cm (for cylindrical geometries); CP and WIMS simulations used $\Delta z = 0.1$ cm and $G = 30$.

The bottom-left graphs of Fig. 3 shows that an increase in $\mathrm{P_N}$ order results in an increase in the k_{eff} calculated by EVENT, with convergence seen at around the 7th order for both geometries.

Finally, Fig. 3 shows that decreasing the radial thickness of cells in EVENT simulations results in an increase in the calculated k_{eff}, with the discretisation reaching convergence when $\Delta r = 0.61$ cm (i.e. 50 divisions in the radial direction).

As shown in Fig. 3, the fully-refined discretisations are consistent across the slab and cylindrical geometries. Table 4 details these discretisations, which will be used for the remainder of the presented research. EVENT will use a Δr of 0.5 cm instead 0.61 cm to enable consistent radial discretisation across the vessel radii investigated.

Table 4
The fully-refined discretisations used in the presented research.

Variable	Fully refined value		
	CP	WIMS	EVENT
Δr (cm)	–	–	0.5
Δz (cm)	0.1	0.1	0.5
G	30	30	30
N	–	–	7

5. Verification of the collision probability code

5.1. Slab models

To verify the slab geometry of the CP code, the parameters of Table 5 were used in all possible combinations, and the resulting k_{eff} and ρ values were compared, in addition to scalar neutron flux distributions in energy ($\phi(E)$) and the distribution of absorption and production rates in energy ($R_A(E)$ and $R_P(E)$) for each material.

The systems investigated consisted of three layers: aqueous at the bottom, organic on the top, and a ‘mixed’ phase in the middle, which was modelled as a homogeneous mixture of the aqueous and organic phases. The composition (as in Table A.11) and thickness (5 cm) of the organic phase remained constant throughout.

5.1.1. Reactivity comparison

In the right-hand graph of Fig. 4, plutonium content, m''_{Pu} (in g cm^{-2}), has been calculated by integrating the system's plutonium concentration, m'''_{Pu} (in g cm^{-3}), along the height, H, of the slab:

$$m'' = \int_0^H dz\, m'''_{\text{Pu}}(z) \tag{32}$$

Table 5
The parameters used in the slab verification.

Variable	Symbol	Parameter values			Unit
Plutonium concentration in the aqueous phase	[Pu]	5.0	50.0	150.0	g L^{-1}
Excess acid molarity in the aqueous phase	[H]	1.0	5.0	10.0	mol L^{-1}
Volume fraction of aqueous in the mixed region	α	0.54	0.60	0.66	–
Thickness of the aqueous layer	h_{aqu}	10.0	15.0		cm
Thickness of the mixed layer	h_{mix}	4.0	8.0		cm

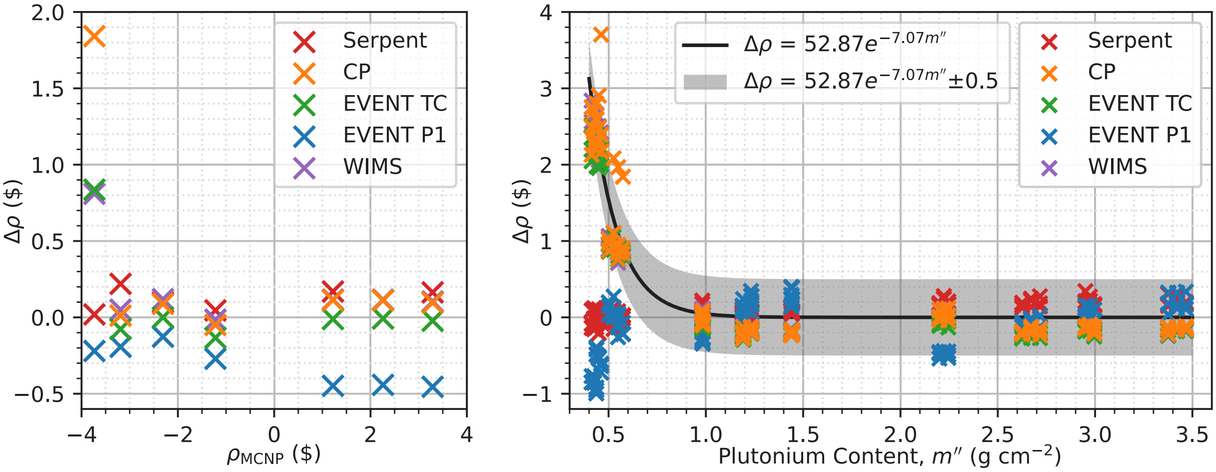

Fig. 4. Variation in $\Delta\rho$ with the reactivities predicted by MCNP (left) and plutonium concentration (right).

As shown in the right-hand graph of Fig. 4, the agreement between the deterministic codes (EVENT, WIMS and CP) and MCNP improves with increasing plutonium content. Throughout all simulations, Serpent agrees to within 0.34 ± 0.26 $ of MCNP, indicating the MC codes are performing as expected and models have been created appropriately.

From the left-hand graph of Fig. 4, it can be seen that, when MCNP predicts a system to be subcritical, the other codes also predict the system to be subcritical. Similarly, when MCNP predicts the system to be prompt supercritical, so do the other codes, with the exception of a single case: when ρ_{MCNP} is 1.22 ± 0.05 $, $\rho_{\mathrm{EVENT\ P1}}$ is 0.77 ± 0.00 $. In addition, the CP code is likely to be accurate to within ~0.2 $ in the critical - prompt supercritical thresholds, but a slight overestimation of reactivity may be observed.

As shown in Fig. 4, the calculated reactivities from the CP code closely match those produced using WIMS, indicating the CP code is performing as expected. Results from the CP code are also similar to those of the EVENT TC calculations, demonstrating there is no advantage of either of the two methods

In the right-hand graph of Fig. 4, it can be seen that increasing the plutonium content decreases $|\Delta\rho|$ exponentially, with some fluctuations seen at higher plutonium contents. To achieve the desired accuracy ($|\Delta\rho| \leq 1.0$ $) for WIMS, CP and EVENT TC calculations, the plutonium content of the slab should be at least 0.7 g cm^{-2}. EVENT P1 calculation of ρ are within the 1.0 $ limit throughout

As such, WIMS, CP and EVENT TC calculation methods are seen to be unsuitable for use modelling systems containing less than 0.6 g cm^{-2} of plutonium (which have ρ_{MCNP} values between −150 and −3.5 $). For WIMS and EVENT TC calculations, $\Delta\rho$ increases from 0.7 to 2.9 $ as plutonium concentration decreases from 0.6 to 0.4 g cm^{-2}. The results from the CP code are similar, though one case yields a notably high error of 3.70 ± 0.39 $ (when $\rho_{\mathrm{MCNP}} = -73.70 \pm 0.28$ $).

The right-hand graph of Fig. 4 shows that the EVENT P1 solutions underpredict system reactivity when there is less than 0.6 g cm^{-2} of plutonium present. However, when compared to the other deterministic codes, there is increased agreement between EVENT P1 solutions and those from MCNP. Thus, it can be postulated that either the transport correction is insufficient for these systems, or there is some error in the isotropic macroscopic neutron cross sections (which were calculated using WIMS).

5.1.2. *Energy and reaction rate comparison*

Fig. 5 depicts the error in scalar neutron flux and aqueous absorption rate, for every system, calculated using the CP code. As shown, whilst the total error in both scalar neutron flux and aqueous absorption rate is consistently below 5%, the maximum error falls below 5% when the plutonium content is higher than 0.7 g cm^{-2}.

Whilst the right-hand graph of Fig. 5 shows only the errors in absorption rate in the aqueous material, the same trends are observed for both absorption and production rates across all materials.

Thus, combined with the results of Section 5.1.1, the CP code can be used to effectively model the behaviour of slab systems containing ≥0.7 g cm^{-2} of plutonium.

Table 6 details, for each code, the highest error in energy-dependent scalar neutron flux and material- and energy-dependent absorption and production rates, when compared to the results from MCNP.

As shown, Serpent predicts all three variables to within ±1.56% of MCNP, further proving the correct and appropriate use of the MC codes.

Across all simulations, the EVENT TC and WIMS calculations of all three variables agree to within ±5.95 and ±5.86% of MCNP, slightly above the required 5%. The EVENT P1 calculations show slightly poorer agreement; within ±8.94% of MCNP. The errors in the CP code results are exceptionally poor, with errors above 100% present in some results.

However, when considering the systems containing at least 0.7 g cm^{-2} of plutonium, the results of all deterministic codes are all acceptable, and agree to within 5% of results calculated using MCNP.

5.2. *Cylindrical models*

To verify the pseudo-cylindrical geometry approximated by the CP code, the same parameters as before, detailed in Table 5, were used, alongside vessel radii (R) of 30.0 and 40.0 cm, and the same layering of aqueous-mixture-organic liquids. Once again, all possible parameter combinations were investigated, and the resulting k_{eff}, ρ, $\phi(E)$, $R_A(E)$ and $R_P(E)$ values were compared.

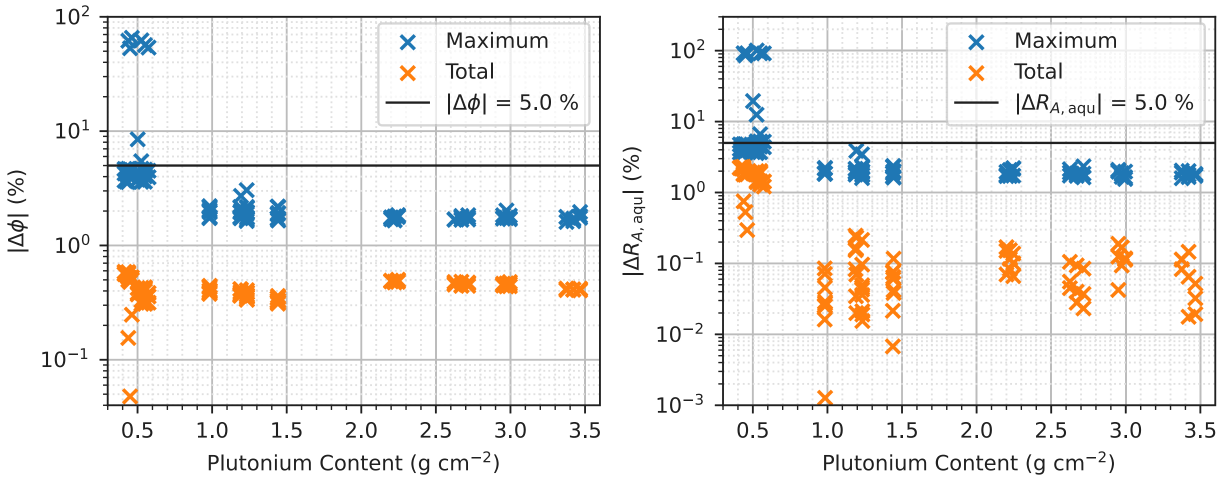

Fig. 5. Errors in the CP code's calculation of scalar neutron flux and aqueous absorption rate, and their variation with plutonium content. The maximum error refers to energy-group-dependent values, and the total error refers to the overall error when integrating the values over the energy spectrum.

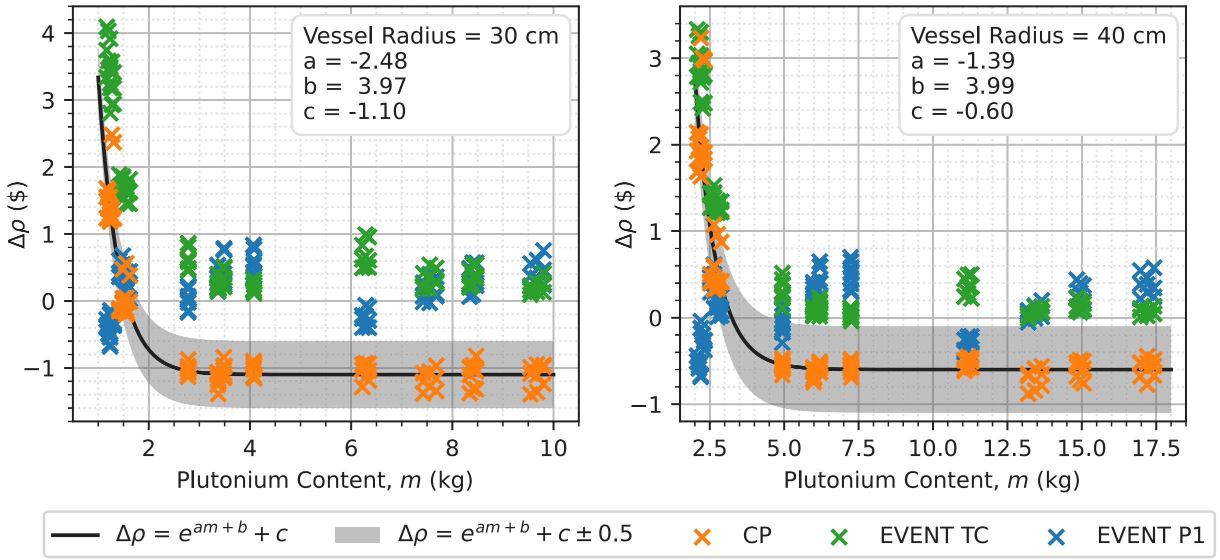

Fig. 6. Variation in $\Delta\rho$ with the mass of plutonium in the system. Results from Serpent have been omitted for figure clarity.

Table 6
The maximum error in energy-dependent scalar neutron flux and material- and energy-dependent absorption and production rates.

Code	Across all simulations			Across simulations with $m'' \geq 0.7$ g cm^{-2}		
	$\Delta\phi$ (%)	ΔR_A (%)	ΔR_P (%)	$\Delta\phi$ (%)	ΔR_A (%)	ΔR_P (%)
Serpent	−1.32 ± 0.04	−1.56 ± 0.08	−1.56 ± 0.09	−1.32 ± 0.04	−1.56 ± 0.08	−1.56 ± 0.09
CP	−65.52 ± 0.07	100.52 ± 0.21	101.39 ± 0.19	−3.05 ± 0.06	−3.87 ± 0.09	−3.88 ± 0.09
EVENT TC	5.26 ± 0.02	5.90 ± 0.03	5.95 ± 0.04	2.19 ± 0.03	−2.92 ± 0.24	−3.14 ± 0.25
EVENT P1	6.73 ± 0.02	8.90 ± 0.03	8.94 ± 0.03	2.28 ± 0.03	2.44 ± 0.04	−2.15 ± 0.24
WIMS	5.23 ± 0.02	5.82 ± 0.03	5.86 ± 0.04	2.21 ± 0.03	−2.81 ± 0.24	−2.84 ± 0.26

5.2.1. Reactivity comparison

Fig. 6 shows the error in deterministic codes' reactivity calculations compared to those of MCNP. Although not shown, Serpent agrees well with MCNP again, with a maximum $|\Delta\rho|$ of 0.49 ± 0.49 $.

Similarly to the slab models, Fig. 6 shows that the $\Delta\rho$ from CP and EVENT TC simulations decreases exponentially with increasing plutonium content, reaching an asymptote for plutonium masses greater than 2.75 kg and 5.0 kg for vessel radii of 30.0 and 40.0 cm, respectively. For the vessels with radii of 30.0 cm, plutonium masses between 2.75 and 10 kg give rise to reactivities between −50 and 60 $. For vessels with radii of 40.0 cm, plutonium masses between 5.0 and 17.5 kg give rise to reactivities between −30 and 75 $.

Conversely, $\Delta\rho$ from EVENT P1 simulations is seen to fluctuate between −0.8 and 0.8 $ across all systems.

As shown in Fig. 6, increasing the vessel radius from 30.0 to 40.0 cm improves the accuracy of EVENT TC simulations: the maximum $\Delta\rho$ decreases from 4.1 $ to 3.3 $, and the range of $\Delta\rho$ in the asymptotic regions decreases from 0.0–1.0 $ to −0.1–0.5 $.

Though the maximum $\Delta\rho$ between the CP code and MCNP increases from 2.5 $ to 3.2 $ when increasing the vessel radius from 30.0 and 40.0 cm, the asymptotic behaviour is improved: the range of $\Delta\rho$ in these regions decreases from −1.4 to −0.8 $ to −0.9 to −0.5 $. This is consistent with the analysis of Section 3.4. In addition, Fig. 6 shows that the CP code is likely to underestimate the reactivities of systems

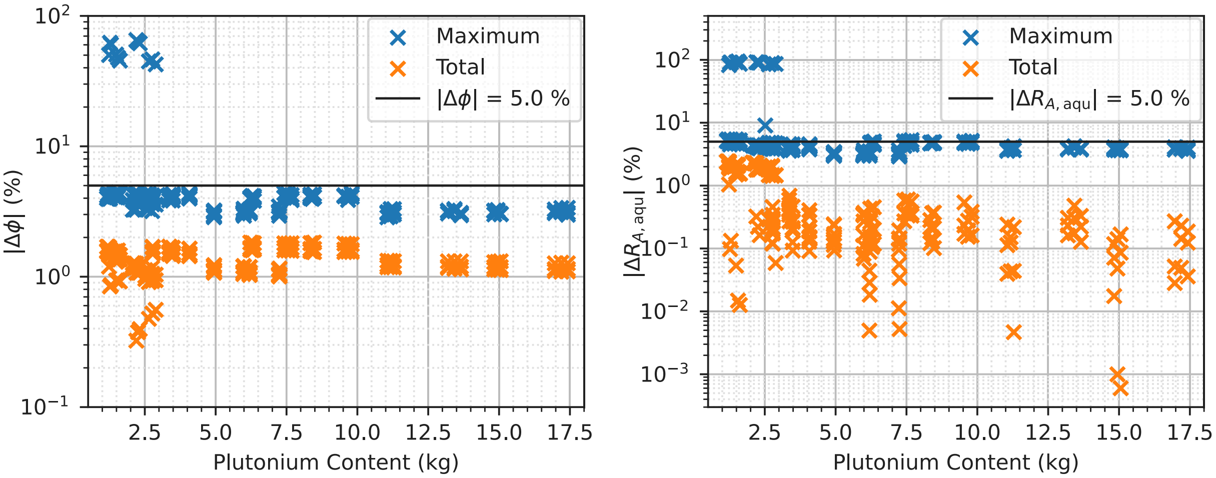

Fig. 7. Errors in the CP code's calculation of scalar neutron flux and aqueous absorption rate, and their variation with plutonium content. The maximum error refers to energy-group-dependent values, and the total error refers to the overall error when integrating the values over the energy spectrum.

with relatively high plutonium contents, indicating overestimation of radial leakage.

Ultimately, as shown in Fig. 6, the difference between MCNP and the CP code's calculation of reactivity is within the 1.0 $ limit for acceptable results when there is at least 5.0 kg of plutonium in vessels with a radius of 40.0 cm. However, the CP code cannot be used to accurately determine the reactivity of vessels with radii of 30.0 cm or below.

5.2.2. Energy and reaction rate comparison

Fig. 7 depicts the error in scalar neutron flux and aqueous absorption rate, for every system, calculated using the CP code. As with the slab models, only the errors in aqueous absorption rate are shown, which are consistently the highest across both absorption and production rates, and the three materials. In addition, the total error in both scalar neutron flux and aqueous absorption rate is consistently below 5%.

However, as shown in Fig. 7, the maximum error in absorption rate is seen to be as high as 100% for systems containing less than 3 kg of plutonium. For systems containing more plutonium, this error is decreased to between 3 and 5%, within the prescribed acceptable range. As before, the same trends are observed for both absorption and production rates across all materials.

A similar trend is seen for the maximum errors in scalar neutron flux: Fig. 7 shows that errors are as high as 65% for systems containing less than 3 kg of plutonium, but consistently below 5% when the plutonium content exceeds 3 kg.

Table 7 details, for each code, the highest error in energy-dependent scalar neutron flux and material- and energy-dependent absorption and production rates, when compared to the results from MCNP.

Though there is slightly poorer agreement between Serpent and MCNP when modelling cylindrical geometries instead of slabs, agreement is still very good, with all Serpent calculations within 1.93% of those from MCNP.

Similarly to the slab geometries, the EVENT TC and EVENT P1 calculations of all three variables agree to within ±5.47 and ±8.82% of MCNP, slightly above the required 5%. When considering all simulations, the errors in the CP code results are again exceptionally poor, with errors up to 94.45%.

Again, when considering the systems containing more plutonium (at least 3 kg for the cylindrical geometries), the results of EVENT TC and EVENT P1 calculations are all acceptable, agreeing to within 5% of MCNP results. The CP results are slightly poorer, just exceeding the 5% limit in the worst cases.

5.2.3. Radial leakage approximation

The results presented in this section indicate that, for systems containing more plutonium (over 2.75 kg and 5.0 kg for vessel radii of 30.0 and 40.0 cm, respectively), the radial leakage approximation employed by the CP code (detailed in Section 3.2) overestimates the rate at which neutrons leak out of the cylinder radially.

This is demonstrated by a tendency of the code to underestimate system reactivity (demonstrated by Fig. 6), and scalar neutron flux and reaction rates (demonstrated by Table 7), for these cases.

5.3. Dished-end models

To verify the use of the CP code to model axially heterogeneous cylinders with dished ends, the parameters detailed in Table 8 were used, alongside $\alpha = 0.6$. The dished ends were modelled as hemispheroids with depth h_{dish}. The layering remains consistent with the previous sections, all possible combinations of parameters were investigated, and the resulting ρ, $\phi(E)$, $R_A(E)$ and $R_P(E)$ values were compared.

5.3.1. Reactivity comparison

The left-hand graph of Fig. 8 shows the error in EVENT's and Serpent's reactivity calculations compared to those of MCNP. Again, Serpent agrees well with MCNP, with a maximum $|\Delta\rho|$ of 0.23 ± 0.08 $, and EVENT P1 calculations of ρ agree to within of 0.72 ± 0.05 $ MCNP, as demonstrated in Fig. 8. The agreement between EVENT TC calculations and MCNP tends to improve as ρ increases, with a maximum $\Delta\rho$ of 2.51 ± 0.49 $, this difference is consistently reduced to 1 $ when ρ_{MCNP} exceeds −25 $.

The right-hand graph of Fig. 8 depicts, for reactivities relatively close to critical, a direct comparison between ρ_{MCNP} and the reactivities calculated using the other codes. For these reactivities, it can be seen that EVENT TC overestimates the reactivity, though all results are within the ±1 $ acceptable range.

The right-hand graph of Fig. 8 also shows that two of the reactivities from the CP code overestimate ρ by over 1.0 $. In these cases, the CP code predicts the systems to be critical and prompt critical when MCNP predicts the systems to be subcritical.

In addition, Fig. 9 shows that there is significant error in some of the reactivities calculated by the CP code, with a maximum difference of 6.37 ± 0.25 $ when compared to MCNP. Although only systems with [H] = 2.5 mol L^{-1} have been plotted, results are very similar (in fact, slightly improved) when [H] = 7.5 mol L^{-1}.

As shown in Fig. 9, the CP code tends to overestimate reactivity, particularly for shorter systems (and thus, in general, systems containing less plutonium). As H_{total} increases, $\Delta\rho_{\mathrm{CP}}$ decreases. Though there

Table 7
The maximum error in energy-dependent scalar neutron flux and material- and energy-dependent absorption and production rates.

Code	Across all simulations			Across simulations with $m \geq 3$ kg		
	$\Delta\phi$ (%)	ΔR_A (%)	ΔR_P (%)	$\Delta\phi$ (%)	ΔR_A (%)	ΔR_P (%)
Serpent	−1.35 ± 0.04	−1.93 ± 0.31	−1.56 ± 0.29	−1.35 ± 0.04	−1.93 ± 0.31	−1.56 ± 0.29
CP	−65.25 ± 0.11	94.40 ± 0.14	94.45 ± 0.14	−4.39 ± 0.13	−5.29 ± 0.20	−5.15 ± 0.29
EVENT TC	5.09 ± 0.02	5.49 ± 0.04	5.47 ± 0.04	2.25 ± 0.03	−3.41 ± 0.32	−3.57 ± 0.24
EVENT P1	6.68 ± 0.02	8.85 ± 0.03	8.82 ± 0.03	2.25 ± 0.03	2.37 ± 0.04	−2.40 ± 0.20

Table 8
The parameters used in the verification of 'dished end' models.

Variable	Symbol	Parameter values			Unit
Plutonium concentration in the aqueous phase	[Pu]	5.0	10.0	–	g L^{-1}
Excess acid molarity in the aqueous phase	[H]	2.5	7.5	–	mol L^{-1}
Thickness of the aqueous layer	h_{aqu}	12.0	17.0	–	cm
Thickness of the mixed layer	h_{mix}	4.0	8.0	–	cm
Thickness of the organic layer	h_{org}	7.5	12.5	–	cm
Vessel radius	R	30.0	40.0	–	cm
Depth of dished end	h_{dish}	5.0	10.0	15.0	cm

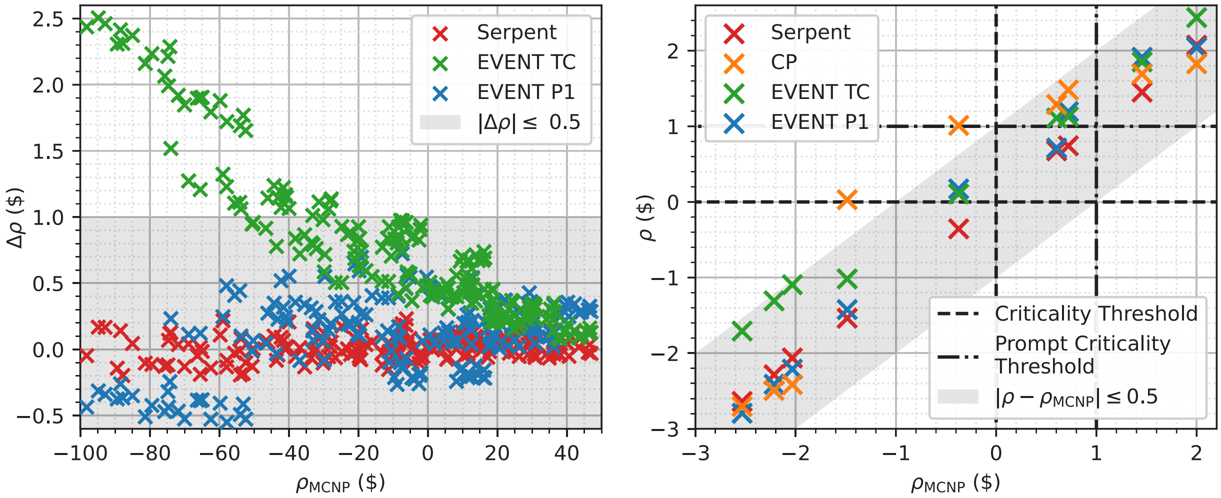

Fig. 8. Left: Variation in $\Delta\rho$ with ρ_{MCNP}, excluding results from the CP code. Right: Reactivities compared to those from MCNP, around the criticality and prompt criticality thresholds.

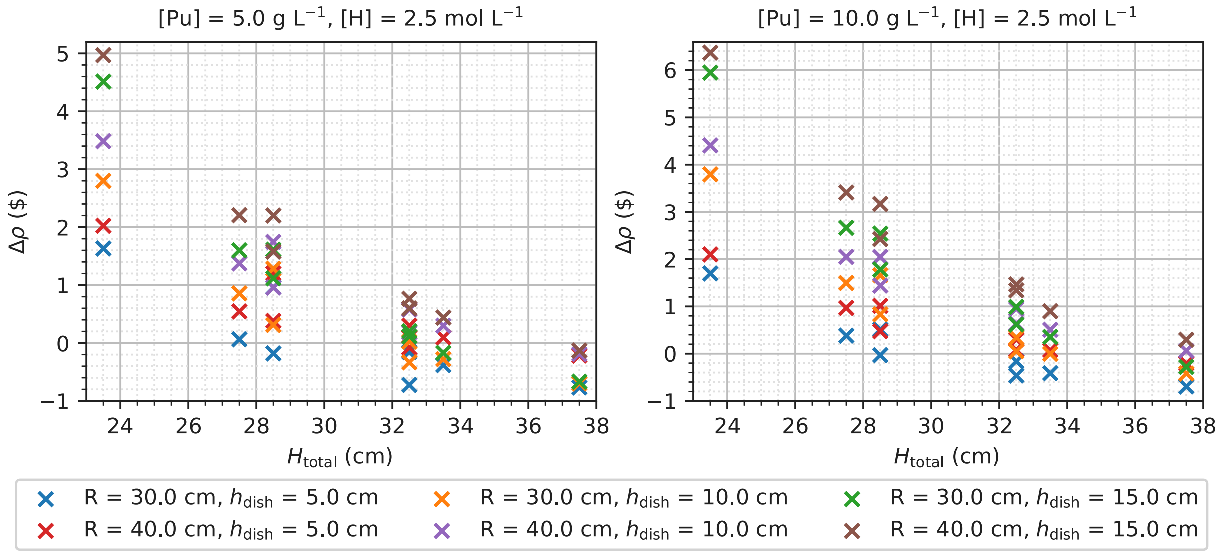

Fig. 9. The variation of $\Delta\rho_{\text{CP}}$ with the total height, H_{total}, of the system.

is some fluctuation in the data, this decrease appears to be exponential; if systems with larger H_{total} were simulated, there is potential for asymptotic behaviour to be seen, as in the previous section.

In addition, Fig. 9 shows that $\Delta\rho_{\text{CP}}$ tends to be larger for systems with larger dished ends and larger radii, with this difference decreasing as H_{total} increases. When there is a higher concentration of plutonium in the aqueous layer, $\Delta\rho_{\text{CP}}$ is increased.

As seen in Fig. 9, there are limited cases in which the CP code can be used to calculate system reactivity to within ±1 \$ of MCNP. For systems with [Pu] = 5.0 g L^{-1}, acceptable results are seen for $H_{\text{total}} \leq 32.0$ cm. For systems with [Pu] = 10.0 g L^{-1} and $R = 40.0$ cm, acceptable results are seen for $H_{\text{total}} \geq 33.5$ cm. For systems with [Pu] = 10.0 g L^{-1} and $R = 30.0$ cm, acceptable results are seen for $H_{\text{total}} \geq 32.0$ cm.

The accuracy of the CP code depends heavily on the height of the vessel's dished end. As shown in Section 3.4, as R/λ increases, the radial leakage approximation used by the CP code becomes more suitable. An increase in h_{dish} means that a more significant portion of the fissile system will have a lower vessel radius, which cannot be modelled as accurately by the CP code. Thus, in general, larger errors are present in results from the CP code when larger portions of the system have small radii, i.e. are part of the dished end.

5.3.2. Energy and reaction rate comparison

Whereas a trend could be seen when plotting $\Delta\rho$ against H_{total}, the error in scalar neutron flux and reaction rates did not show the same trend.

Fig. 10 shows how the errors in the CP code for calculations of total and maximum ϕ and $R_{A,\text{aqu}}$ vary with the quantity of plutonium in the system.

The top-left graph of Fig. 10 shows four distinct regions of data, for plutonium masses in the ranges 1.5–2.1 kg, 2.3–2.9 kg, 2.5–3.8 kg and 4.1–5.2 kg. For each region, both maximum and total values of $|\Delta\phi|$ are seen to decrease with increasing plutonium content. Total errors are less than 5% throughout, though there are only limited cases, when $h_{\text{dish}} = 5.0$ cm, where the maximum error is below 5%.

Some improvement in results is seen when increasing h_{aqu} from 12.0 to 17.0 cm: as shown in the top-right graph of Fig. 10, all total errors are less than 5%, most maximum errors are below 5% when $h_{\text{dish}} = 5.0$ cm, and, when $h_{\text{dish}} = 10.0$ cm, a limited number of maximum errors are below 5% .

As with previous sections, Fig. 10 depicts $|\Delta R_{A,\text{aqu}}|$ over errors in other material-wise absorption and production rates as CP code calculations of $R_{A,\text{aqu}}$ are associated with the highest errors. Also with previous sections, errors in absorption and production rates across all materials show similar trends to those in $R_{A,\text{aqu}}$. In addition, R_A is always overestimated by the CP code, whereas R_P is overestimated when system reactivity is overestimated.

As depicted in Fig. 10, errors increase slightly with increasing plutonium content. All of the maximum errors in $R_{A,\text{aqu}}$ are above the 5% limit of acceptability. When considering total $R_{A,\text{aqu}}$ across all energy, the CP code can only consistently calculate values to within 5% of MCNP when $h_{\text{dish}} = 5.0$ cm.

Fig. 11 depicts, for an example system, the distribution of ϕ, R_A and R_P in energy, with R_A and R_P also distributed across the three materials.

Fig. 11 shows that $\Delta\phi_{\text{CP}}$ is largest for neutrons in energy group 29 (with energies between 0.134 and 0.248 eV) and smallest for neutrons in energy group 1 (with energies between 6.70 and 19.6 MeV), whilst $|\Delta\phi_{\text{CP}}|$ is smallest for neutrons in energy group 27 (with energies between 0.391 and 0.625 eV). The axial scalar neutron flux distributions for these energy groups are depicted in Fig. 12.

Similarly, the highest error associated with the CP code's calculation of $R_A(E)$ and $R_P(E)$ occurs for neutrons in the aqueous material and in the 29th energy group, with $\Delta R_{A,\text{aqu}}(E)$ and $\Delta R_{P\text{aqu}}(E)$ having maxima of 11.77 ± 0.05% and 11.79 ± 0.05% respectively.

To complement Figs. 10, 11 shows that, even though errors can be significantly high for energy- and material-dependent values of $\phi(E)$, $R_A(E)$ and $R_P(E)$, the total error when taken over energy and material is acceptably small, with the largest total error, ΔR_A, being 0.67 ± 0.02 \$. This is due to the overestimate of $\phi(E)$, $R_A(E)$ and $R_P(E)$ at lower energies and in the aqueous material being counteracted by underestimates at higher energies and in the organic and mixture regions.

As shown in Fig. 12, the CP code accurately predicts the location of the peaks in scalar neutron flux.

Fig. 12 shows that, for group 1, the CP code underestimates the peak magnitude by around 0.09×10^{-6} neutrons cm^{-2} s^{-1}, or around 4.2%. In addition, the magnitude ϕ_1 is overestimated in the dished end ($0 \leq z \leq 5$ cm). Elsewhere, the shape of the profile closely matches that produced using MCNP.

For energy group 27, Fig. 12 shows that the CP codes again overestimates the scalar neutron flux in the dished end, though there is excellent agreement with MCNP throughout the rest of the system.

Finally, Fig. 12 shows that, though the shape of the flux profile in energy group 29 is similar to that produced using MCNP, the CP code overestimates the flux in the range ($0 \leq z \leq 25$ cm), and is particularly notable up to the second peak in flux. The peaks' magnitudes have been overestimated by the CP code by around 4.2% and 2.8% respectively.

5.4. Complete vessel models

In this section, models of complete vessels with dished tops and bottoms were investigated. For each individual system, the vessel's top and bottom dished ends were the same shape and size (i.e. had the same h_{dish}), the vessel walls were modelled as 1 cm thick steel, and the total vessel height (H_{vess}) was kept constant at 50.0 cm. The vessel radius and height, R and H_{vess}, were taken at the inner wall of the vessel. Once again, the same material layering as previous sections were used, with the remainder of the vessel filled with air at atmospheric pressure. The same parameters as Section 5.3 were used, and are detailed in Table 8.

5.4.1. Reactivity comparison

As with the previous section, Fig. 13 shows the error in EVENT's and Serpent's reactivity calculations compared to those of MCNP, for the whole range of system reactivities in the left-hand graphs, and for reactivities relatively close to critical in the right-hand graph.

When compared to the geometrically less complex models, there is slightly poorer agreement between Serpent and MCNP, with a maximum $|\Delta\rho|$ of 1.10 ± 0.42 \$. However, Fig. 13 shows that the majority of Serpent's results are within the acceptable range ($|\Delta\rho| \leq 0.5$ \$), including systems with reactivities close to critical

As shown in Fig. 13, both EVENT TC and P1 calculations underestimate system reactivity when compared to MCNP, with agreement improving with increasing ρ_{MCNP}. However, for both TC and P1 calculations, the majority of systems are calculated with $|\Delta\rho| > 1.0$ \$, outside the acceptable range.

The right-hand graph of Fig. 13 shows that, for systems around criticality, there can be significant error present when modelling complete vessels of fissile liquids in the CP code, with the CP code overestimating system reactivity. For example, when MCNP predicts a system to be subcritical (with ρ_{MCNP} of −5.08 ± 0.03 \$), the CP code predicts it to be critical (with ρ_{CP} of 0.31 \$).

Further, Fig. 14 shows that $\Delta\rho_{\text{CP}}$ decreases with increasing plutonium content. As shown, the CP code consistently overestimates the reactivity of systems containing a relatively small amount of plutonium, such that there are only a few cases in which the CP code can be used to accurately determine system reactivity: mostly, $\Delta\rho_{\text{CP}} > 1.0$ \$, and the maximum difference between the CP code and MCNP is 12.29 ± 0.31 \$.

The graphs of Fig. 14 show that, for systems with vessel radii of 30.0 cm, 2.5–3.0 kg of plutonium needs to be present in the system for the CP code to be likely to calculate the reactivity to the required

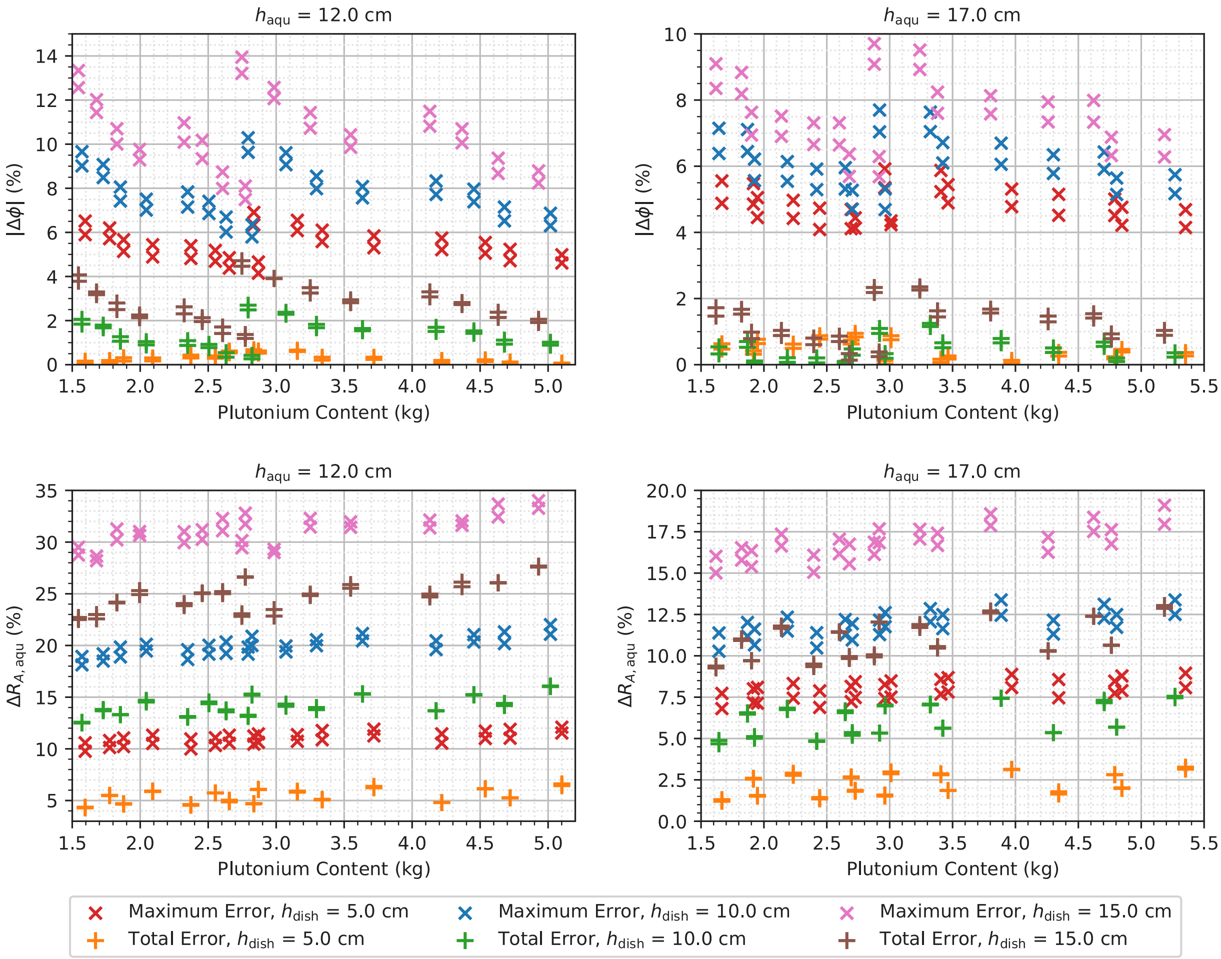

Fig. 10. The maximum (across all energy groups and materials) and total errors in the CP code's calculations of ϕ and $R_{A,\text{aqu}}$, plotted against system plutonium content.

accuracy. Even with this limit on parameters, there are a few cases (with h_{dish} = 15.0 cm) which have $\Delta\rho_{\text{CP}} > 1.0$ \$.

Finally, as shown in Fig. 14, when the vessel radius is increased to 40.0 cm, there are only five cases where the CP code calculates the system reactivity to within ±1.0 \$ of MCNP which all occur at the highest plutonium content.

5.4.2. Energy and reaction rate comparison

Fig. 15 shows how the errors in the CP code's calculations of $R_{A,\text{aqu}}$ vary with plutonium content.

As depicted in Fig. 15, when h_{aqu} is 12 cm, the maximum error, taken over all groups, is always above the 5% acceptable limit. When h_{aqu} is 17 cm, the maximum error is only under 5% when the plutonium content is less than 2.7 kg, and h_{dish} = 5.0 cm.

Fig. 15 also demonstrates that, when h_{aqu} is 12 cm, the total error is only within this limit for systems with h_{dish} = 5.0 cm. When h_{aqu} is 17 cm, the total error is within the 5% limit for systems with h_{dish} equal to 5.0 or 10.0 cm.

As with previous sections, Fig. 15 only shows the errors in aqueous absorption rate calculation, with similar patterns observed for absorption and production rates across all materials. The errors in aqueous production rates are on a similar scale to the aqueous absorption rates shown in Fig. 15. Conversely, the total errors in absorption and production rates for the mixed and organic layer are all below the 5% limit, with maximum errors between 0.2 and 9%.

The left-hand graph of Fig. 16 depicts the axial variation in total scalar neutron flux for the system described in Table 9. As shown the CP code fails to model the decrease in scalar neutron flux in the range $24.5 \le z \le 51.0$ cm, i.e. through the region of plenum gas at the top of the vessel.

Table 9
The system parameters producing the scalar neutron flux profiles in Figs. 16 and 17.

Parameter	Value	Unit
[Pu]	10.0	g L^{-1}
[H]	7.5	mol L^{-1}
h_{aqu}	12.0	cm
h_{mix}	4.0	cm
h_{org}	7.5	cm
R	40.0	cm
h_{dish}	15.0	cm

As such, the errors in scalar neutron flux are significantly high, as shown in the right-hand graph of Fig. 16. In this graph, all errors are positive, indicating the CP code overestimates the scalar neutron flux, all maximum errors are above the 5% limit, and only a small number of total errors are below the 5% limit (for the highest plutonium contents for each of the vessel radii).

In addition, as shown in the left-hand graph of Fig. 16, the CP code slightly overestimates the scalar neutron flux in the base of the vessel and through the dished end ($0.0 \le z \le 16.0$ cm). This is a trend seen throughout the systems investigated, and explains why the majority of aqueous absorption rates detailed in Fig. 15 are positive (indicating the CP code has overestimated these values).

Conversely, the flux profile produced from the CP code matches MCNP and Serpent well for $16.0 \le z \le 24.5$ cm. The location and magnitude of the peak scalar neutron flux is accurately predicted to

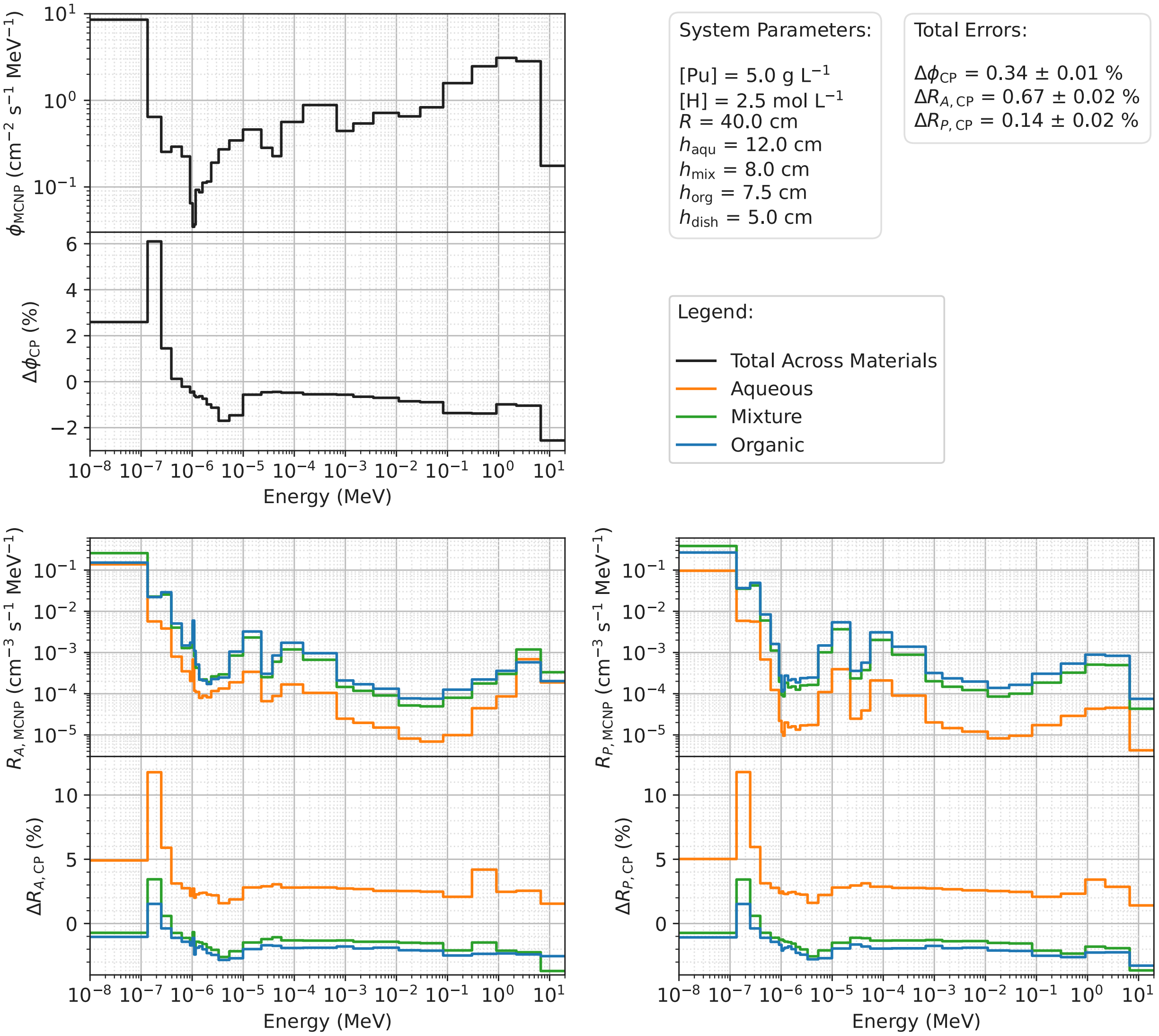

Fig. 11. The errors in CP code calculations of $\phi(E)$, $R_A(E)$ and $R_P(E)$, for the example system detailed.

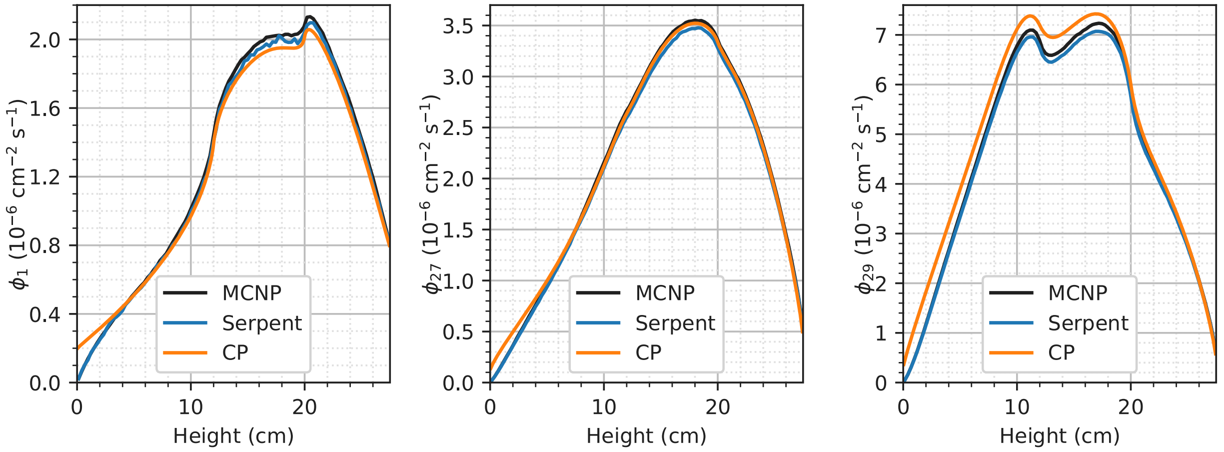

Fig. 12. Radially averaged axial scalar neutron flux distributions for energy groups 1 (left), 27 (centre) and 29 (right), for the system described in Fig. 11.

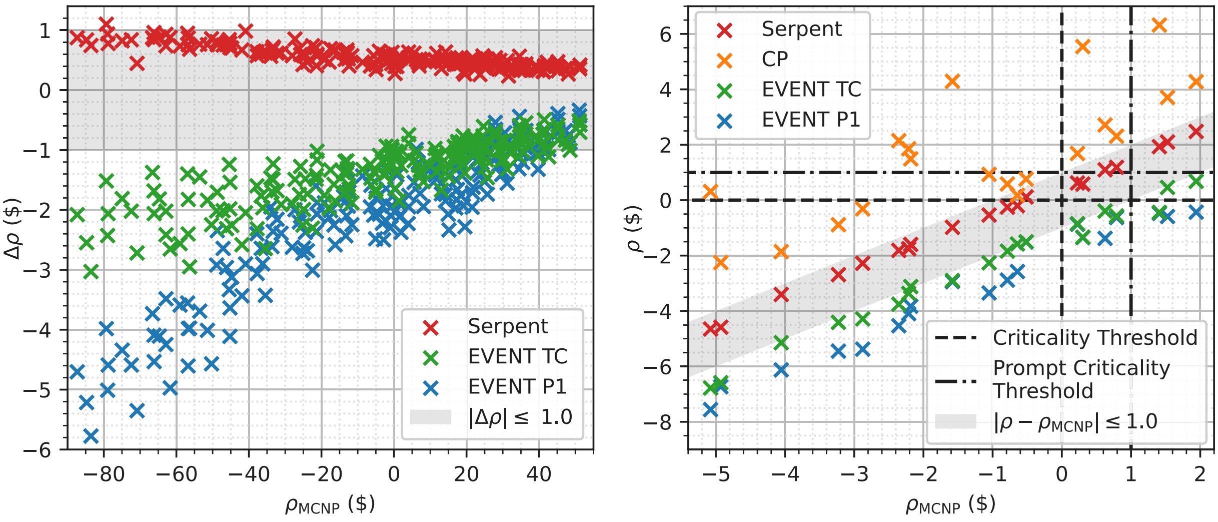

Fig. 13. Left: Variation in $\Delta\rho$ with ρ_{MCNP}, excluding results from the CP code. Right: Reactivities compared to those from MCNP, around the criticality and prompt criticality thresholds.

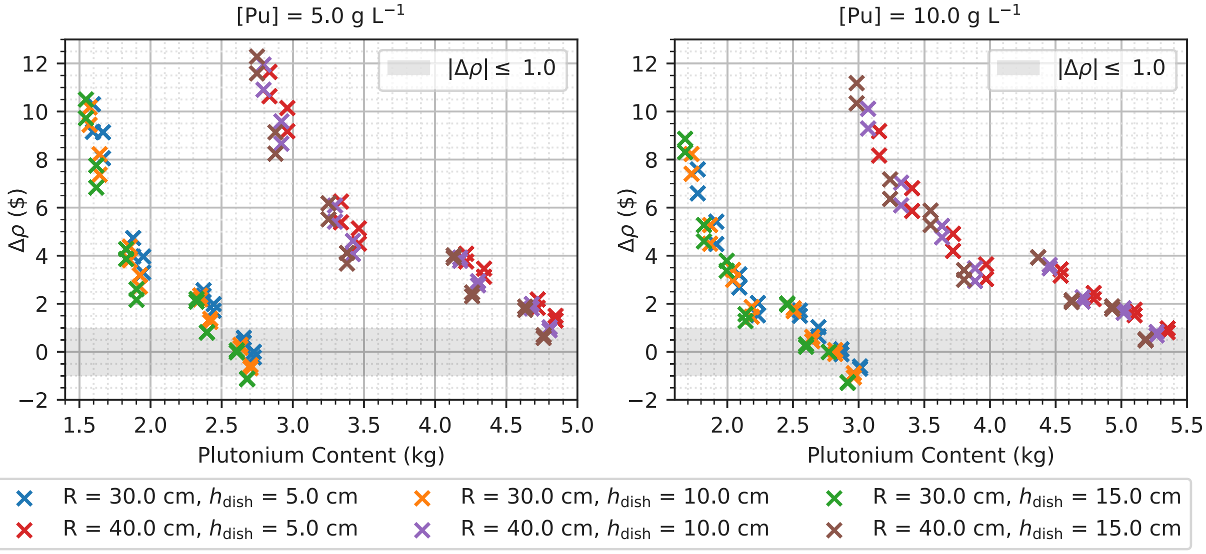

Fig. 14. The variation of $\Delta\rho_{\mathrm{CP}}$ with the total plutonium content of the system.

be around 3.05×10^{-4} neutrons $\mathrm{cm}^{-2}\ \mathrm{s}^{-1}$ around 15.5 cm from the base of the system.

When considering the scalar neutron flux in the fissile regions only, Fig. 17 shows there is improved agreement between the CP code and MCNP, such that all total errors are now within the 5% acceptable limit. However, maximum errors were still as high as 12%.

5.4.3. Summary

As shown in this Section, significant care is needed when using the CP code to model full vessels with dished ends. The CP code failed to adequately model many of the systems simulated.

For both vessel radii used, the CP code could only calculate reactivity to within 1 $ of MCNP when plutonium content was at its highest. However, increasing plutonium content tended to increase the error in the CP code's calculations of aqueous absorption rate.

As the CP code tends to overestimate the reactivities of the full vessel systems, a subcritical system could be calculated to be critical or even supercritical by the CP code, which would significantly alter system characteristics or any subsequent analysis performed using the code's results.

Finally, when using the CP code, only the parts of the scalar neutron flux profiles in the fissile regions should be used (i.e. the scalar neutron flux through any plenum gas should be deemed inaccurate and not used for further analysis).

6. Conclusions

This paper presented the development and verification of a CP code for systems of layered fissile liquids (aqueous and organic plutonium nitrate at the top and bottom with a mixed central region).

To model axially heterogeneous cylinders using the CP code whilst maintaining the computationally efficient nature of a one dimensional slab model, an approximation based on diffusion theory was used, which employed the neutron diffusion coefficient and geometric buckling to determine the rate of radial leakage of neutrons from the system, which was added to the system's macroscopic neutron absorption cross sections.

To verify this approximation, results from the CP code were compared to MCNP. Results compared included reactivity, neutron absorption and production rates across energy and material, and scalar neutron flux profiles across energy and system height.

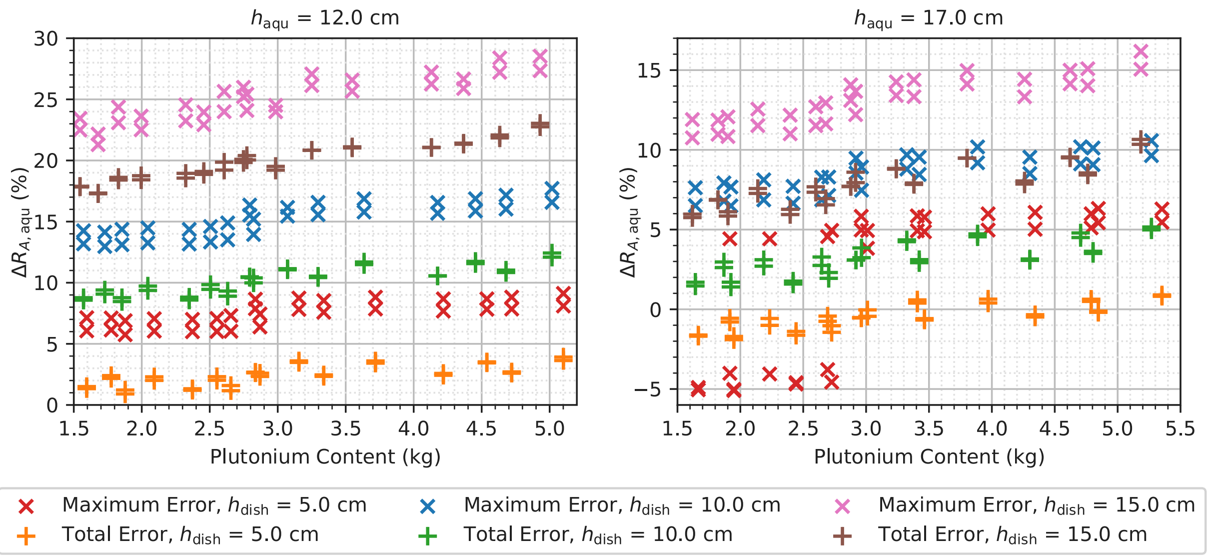

Fig. 15. The maximum (across all energy groups and materials) and total errors in the CP code's calculations of $R_{A,\text{aqu}}$, plotted against system plutonium content.

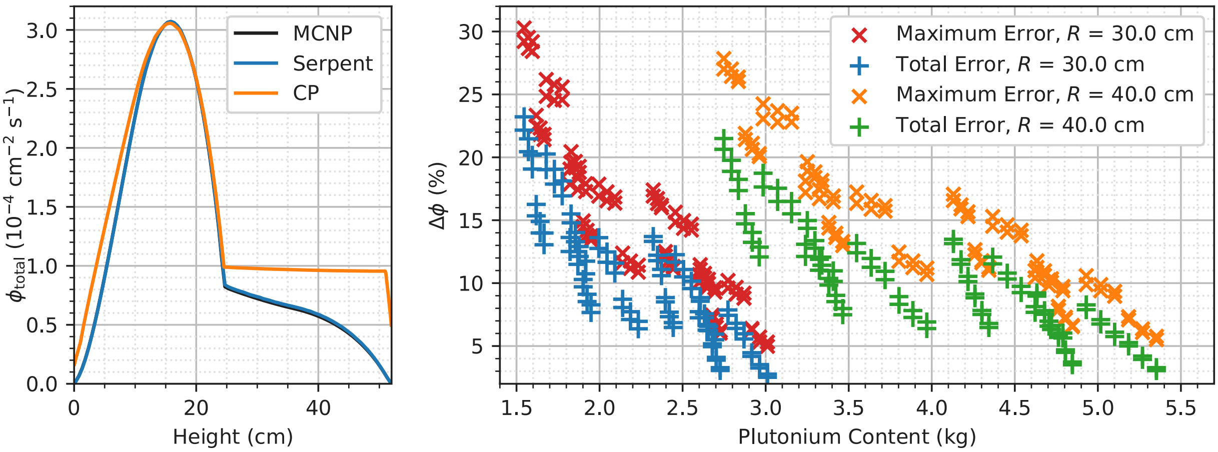

Fig. 16. Left: radially averaged axial scalar neutron flux distribution totalled over all energy groups, for the system described in Table 9. Right: for all systems, the variation in maximum (across all energy groups) and total errors in scalar neutron flux with system plutonium content.

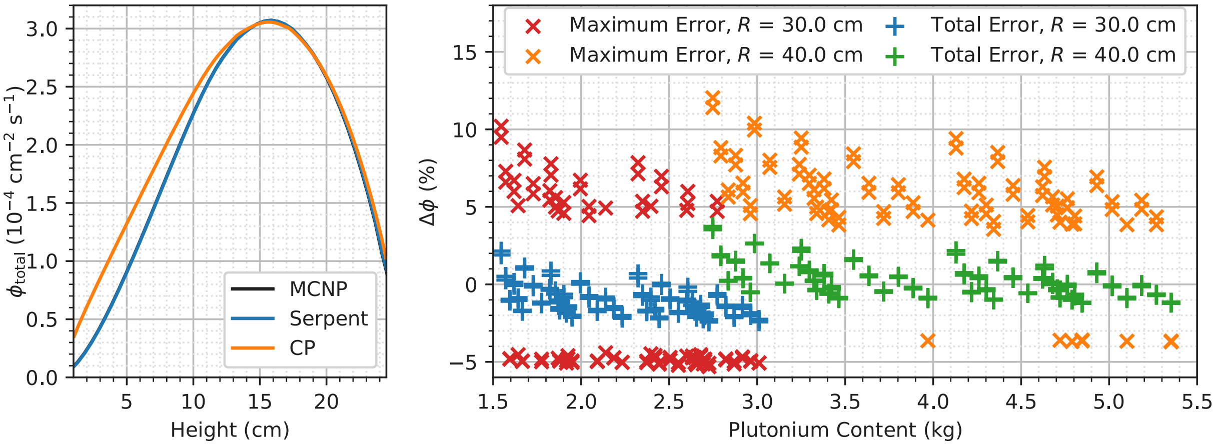

Fig. 17. Left: radially averaged axial scalar neutron flux distribution totalled over all energy groups, for the system described in Table 9, considering the fissile regions only. Right: for all systems, considering the fissile regions only, the variation in maximum (across all energy groups) and total errors in scalar neutron flux with system plutonium content.

When modelling slab geometries, the CP code tended to match the results from the reactor physics code WIMS closely, indicating that the CP method was implemented correctly.

Slab geometries needed to contain at least 0.7 g cm^{-2} plutonium for the CP code to calculate reactivity to within 0.4 \$, and reaction rates to within 4% of MCNP, within the prescribed levels of numerical accuracy.

For cylindrical geometries, increasing the plutonium content caused $\Delta\rho_{\mathrm{CP}}$ to decrease to an asymptotic value. For cylinders with 30 cm radii, this asymptotic value was ~ -1.1 \$, outside of the prescribed level of numerical accuracy. Increasing the vessel radii to 40 cm, increased the asymptotic value to ~ -0.6 \$, within the prescribed level of numerical accuracy.

The cylindrical models needed to contain at least 3 kg of plutonium for the CP code to calculate the energy dependent scalar neutron flux and energy and material dependent neutron absorption and production rates to within 5.3% of MCNP, just outside of the prescribed level of numerical accuracy.

As detailed in Section 3.4, the radial leakage approximation is more suitable for vessels with larger radii, which was demonstrated in Section 5.2: increasing vessel radius from 30.0 to 40.0 cm increased the agreement between MCNP and the CP code's reactivities by up to 0.6 \$. It was concluded that the approximation used to model axially heterogeneous cylinders in the CP code overestimated the rate of radial neutron leakage.

When incorporating a dished end to the cylindrical models, the agreement between the CP code and MCNP worsened, with $\Delta|rho_{\mathrm{CP}}$ decreasing with increasing system height. For systems with 5.0 g L^{-1} of plutonium in the aqueous phase, a total height of at least 32 cm was needed for ρ to be within 1 \$ of MCNP. When the plutonium content increased to 10.0 g L^{-1}, the total height needed to be at least 33.5 cm.

For these models, error increased with dish height, and the maximum errors in reaction rates and scalar neutron fluxes were frequently higher than 5%. However, when taken over all energy, the total errors in scalar neutron flux were consistently within 5% of MCNP. For total reaction rates, the CP code could only calculate reaction rates to within 5% of MCNP for systems with dish heights of 5.0 cm.

The overestimation of absorption and production rates in the aqueous material were was counteracted by underestimates in absorption and production rates in the mixed and organic regions. The energy dependent, radially averaged axial scalar neutron flux was calculated accurately by the CP code. The location of the peaks in scalar neutron flux matched those from MCNP, with magnitudes matching to within 5%.

When modelling full vessels, there were very limited cases in which the CP code could be used to achieve results to the desired level of accuracy across all variables investigated.

Only in select cases did the CP code calculate reactivity to within 1 \$ of MCNP, and the total aqueous absorption and production rate were only within 5% of MCNP when the dish height was 5.0 cm, or when the dish height was 10.0 cm and the aqueous height was 17.0 cm.

Further, the CP code failed to accurately calculate the decrease in scalar neutron flux through the plenum gas at the top of the vessel, inducing larger errors in scalar neutron flux compared to the geometrically simpler models.

As such, the CP code should be used with increasing caution when the geometric complexity of the system increases, with overestimations of reactivity likely. Energy and material-dependent reaction rates could be highly erroneous, though total rates are likely to be accurate.

As a simple, neutronics based model, the CP code could be used as part of rough order of magnitude calculations for criticality transients, where high levels of accuracy are not required, given that potential errors in results have been previously identified.

CRediT authorship contribution statement

J.R. Daniels: Conceptualization, Data curation, Formal analysis, Methodology, Software, Validation, Visualization, Writing – original draft, Review & editing. **M.M.R. Williams:** Conceptualization, Methodology, Supervision, Writing – review & editing. **M.D. Eaton:** Conceptualization, Funding acquisition, Methodology, Project administration, Resources, Supervision, Writing – review & editing.

Declaration of competing interest

The authors declare that they have no known competing financial interests or personal relationships that could have appeared to influence the work reported in this paper.

Data availability

In accordance with EPSRC funding requirements, all supporting data used to create figures in this paper may be accessed at the following doi: 10.17632/7tmv36spxp.1.

Table A.10
The atomic composition of the aqueous material used in Section 4 (Chalmers, 1971).

Nuclide	Atomic weight	Aqueous		
		Number density (atoms barn^{-1} cm^{-1})	Weight %	Atomic %
Hydrogen	1.0080	5.909×10^{-2}	7.750	56.986
Nitrogen	14.0067	4.287×10^{-3}	7.812	4.134
Oxygen	15.9994	4.030×10^{-2}	83.889	38.862
^{239}Pu	239.0522	1.653×10^{-5}	0.514	0.016
^{240}Pu	240.0540	1.098×10^{-6}	0.034	0.001

Table A.11
Atomic compositions of the mixed and organic materials used in Section 4 (Chalmers, 1971).

Nuclide	Atomic weight	Organic			Mixture A		
		Number density (atoms barn^{-1} cm^{-1})	Weight %	Atomic %	Number density (atoms barn^{-1} cm^{-1})	Weight %	Atomic %
Hydrogen	1.0080	6.090×10^{-2}	10.671	61.744	5.991×10^{-2}	8.869	59.085
Carbon	12.0112	3.187×10^{-2}	66.550	32.314	1.445×10^{-2}	25.500	14.256
Nitrogen	14.0067	7.710×10^{-4}	1.877	0.782	2.692×10^{-3}	5.538	2.655
Oxygen	15.9994	4.423×10^{-3}	12.302	4.484	2.403×10^{-2}	56.459	23.696
Phosphorus	30.9738	5.274×10^{-4}	2.840	0.535	2.392×10^{-4}	1.088	0.236
^{239}Pu	239.0522	1.299×10^{-4}	5.399	0.132	6.796×10^{-5}	2.386	0.067
^{240}Pu	240.0540	8.625×10^{-6}	0.360	0.009	4.512×10^{-6}	0.159	0.004

Table A.12
Densities of the three materials of Section 4 (Chalmers, 1971).

Material	Density (g cm^{-3})
Aqueous	1.276
Organic	0.955
Mixture A	1.130

Table B.13
The discretisation (energy group boundaries) used for the 2-group energy structure.

Group	Upper energy boundary (eV)
1	1.96×10^{7}
2	9.72×10^{-1}

Table B.14
The discretisation (energy group boundaries) used for the 8-group energy structure.

Group	Upper energy boundary (eV)	Group	Upper energy boundary (eV)
1	1.96×10^{7}	5	9.17×10^{1}
2	8.21×10^{5}	6	9.91×10^{0}
3	2.93×10^{4}	7	1.02×10^{0}
4	1.01×10^{3}	8	5.80×10^{-2}

Table B.15
The discretisation (energy group boundaries) used for the 20-group energy structure.

Group	Upper energy boundary (eV)	Group	Upper energy boundary (eV)	Group	Upper energy boundary (eV)
1	1.96×10^{7}	8	1.01×10^{3}	15	1.76×10^{0}
2	4.49×10^{6}	9	2.04×10^{2}	16	1.24×10^{0}
3	8.21×10^{5}	10	5.56×10^{1}	17	1.02×10^{0}
4	1.11×10^{5}	11	3.37×10^{1}	18	5.40×10^{-1}
5	2.93×10^{4}	12	1.59×10^{1}	19	2.20×10^{-1}
6	9.12×10^{3}	13	7.52×10^{0}	20	5.80×10^{-2}
7	2.25×10^{3}	14	2.60×10^{0}		

Table B.16
The discretisation (energy group boundaries) used for the 30-group energy structure.

Group	Upper energy boundary (eV)	Group	Upper energy boundary (eV)	Group	Upper energy boundary (eV)
1	1.96×10^{7}	11	6.77×10^{2}	21	1.59×10^{0}
2	6.70×10^{6}	12	1.49×10^{2}	22	1.37×10^{0}
3	2.23×10^{6}	13	5.56×10^{1}	23	1.17×10^{0}
4	9.07×10^{5}	14	3.73×10^{1}	24	1.10×10^{0}
5	3.02×10^{5}	15	2.26×10^{1}	25	1.02×10^{0}
6	8.23×10^{4}	16	9.91×10^{0}	26	9.10×10^{-1}
7	2.93×10^{4}	17	5.35×10^{0}	27	6.25×10^{-1}
8	1.11×10^{4}	18	3.30×10^{0}	28	3.91×10^{-1}
9	3.53×10^{3}	19	2.36×10^{0}	29	2.48×10^{-1}
10	1.43×10^{3}	20	1.93×10^{0}	30	1.34×10^{-1}

Acknowledgements

UK Ministry of Defence © Crown owned copyright 2023/AWE. Ms. J.R. Daniels gratefully acknowledges the financial support of the Engineering and Physical Science Research Council (EPSRC) and AWE, United Kingdom plc through the industrial CASE PhD programme (EPSRC Grant No.: EP/T517690/1), and the comments and reviews from Mr. G.S. Jones.

Appendix A. Material properties used in the presented research

See Tables A.10–A.12.

Appendix B. Energy group structures

See Tables B.13–B.16.

References

Askew, J.R., Fayers, F.J., Kemshell, P.B., 1966. General description of the lattice code WIMS. J. Br. Nucl. Energy Soc. 5, 564–585.

Askew, J.R., Roth, M.J., 1982. WIMS-E. Technical Report AEEW-R–1315, UKAEA Atomic Energy Establishment, Winfrith.

Bell, G.I., Hansen, G.E., Sandmeier, H.A., 1967. Multitable treatments of anisotropic scattering in S_N multigroup transport calculations. Nucl. Sci. Eng. 28 (3), 376–383.

Bizet, R., Lévêque, F., 2017. Resilience: A new paradigm of nuclear safety. In: Ahn, J., Guarnieri, F., Furuta, K. (Eds.), Chapter the Economic Assessment of the Cost of Nuclear Accidents. Springer, pp. 79–96.

Brown, D., Chadwick, M., Capote, R., Kahler, A., Trkov, A., Herman, M., Sonzogni, A., Danon, Y., Carlson, A., Dunn, M., Smith, D., Hale, G., Arbanas, G., Arcilla, R., Bates, C., Beck, B., Becker, B., Brown, F., Casperson, R., Conlin, J., Cullen, D., Descalle, M.-A., Firestone, R., Gaines, T., Guber, K., Hawari, A., Holmes, J., Johnson, T., Kawano, T., Kiedrowski, B., Koning, A., Kopecky, S., Leal, L., Lestone, J., Lubitz, C., Márquez Damián, J., Mattoon, C., McCutchan, E., Mughabghab, S., Navratil, P., Neudecker, D., Nobre, G., Noguere, G., Paris, M., Pigni, M., Plompen, A., Pritychenko, B., Pronyaev, V., Roubtsov, D., Rochman, D., Romano, P., Schillebeeckx, P., Simakov, S., Sin, M., Sirakov, I., Sleaford, B., Sobes, V., Soukhovitskii, E., Stetcu, I., Talou, P., Thompson, I., van der Marck, S., Welser-Sherrill, L., Wiarda, D., White, M., Wormald, J., Wright, R., Zerkle, M., Žerovnik, G., Zhu, Y., 2018. ENDF/B-VIII.0: The 8th major release of the nuclear reaction data library with CIELO-project cross sections, new standards and thermal scattering data. Nucl. Data Sheets 148, 1–142, Special Issue on Nuclear Reaction Data.

Cacuci, D.G. (Ed.), 2010. Handbook of Nuclear Engineering. Springer Science+Business Media LLC.

Carlvik, I., 1966. Integral Transport Theory in One-dimensional Geometries. Technical Report AE-227, AB Atomenergi, Nykoeping.

Chadwick, M., Herman, M., Obložinský, P., Dunn, M., Danon, Y., Kahler, A., Smith, D., Pritychenko, B., Arbanas, G., Arcilla, R., Brewer, R., Brown, D., Capote, R., Carlson, A., Cho, Y., Derrien, H., Guber, K., Hale, G., Hoblit, S., Holloway, S., Johnson, T., Kawano, T., Kiedrowski, B., Kim, H., Kunieda, S., Larson, N., Leal, L., Lestone, J., Little, R., McCutchan, E., MacFarlane, R., MacInnes, M., Mattoon, C., McKnight, R., Mughabghab, S., Nobre, G., Palmiotti, G., Palumbo, A., Pigni, M., Pronyaev, V., Sayer, R., Sonzogni, A., Summers, N., Talou, P., Thompson, I., Trkov, A., Vogt, R., van der Marck, S., Wallner, A., White, M., Wiarda, D., Young, P., 2011. ENDF/B-VII.1 nuclear data for science and technology: Cross sections, covariances, fission product yields and decay data. Nucl. Data Sheets 112 (12), 2887–2996, Special Issue on ENDF/B-VII.1 Library.

Chalmers, J.H., 1971. Calculations Relating to the Criticality Incident at Windscale on the 24 August 1970. Technical Report AHSB(S)R.195.

Chiba, G., 2004. Effect of neutron anisotropic scattering and treatment of angular dependency of neutron flux in effective cross section on criticality in fast reactor analysis. Trans. At. Energy Soc. Japan 3 (2), 200–207.

Conlin, J.L., Parsons, D.K., Gardiner, S.J., Kahler, III, A.C., Lee, M.B., White, M.C., Gray, M.G., 2013. Continuous energy neutron cross section data tables based upon ENDF/B-VII.1. (LA-UR-13-20137), Los Alamos National Laboratory (LANL), Los Alamos, New Mexico, USA, http://dx.doi.org/10.2172/1063914.

Coulson, S.G., 1999. Generating Nuclear Data for WIMS - The NJOY Module WIMSR (University of Birmingham Master's thesis, under sponsorship from Atomic Energy Authority Technology - Report No. AEAT-6093).

Crossland, I. (Ed.), 2012. Nuclear Fuel Cycle Science and Engineering. Woodhead Publishing Series in Energy, Woodhead Publishing Ltd.

de Oliveira, C.R.E., 1987. Finite Element Techniques for Multigroup Neutron Transport Calculations with Anisotropic Scattering (Ph.D. thesis). Queen Mary University of London.

de Oliveira, C.R.E., 2001a. EVENT: A Multigroup, Finite Element-Spherical Harmonics Program for the Solution of Steady-State and Time-Dependent Radiation Transport Problems in Arbitrary Geometry. Imperial College of Science, Technology and Medicine.

de Oliveira, C.R.E., 2001b. GEM: A Finite Element Mesh Generator and Data Preparation Program for Radiation Transport and Fluids Codes. Imperial College London.

Dean, C.J., 1993. Production of Application Libraries for WIMS. Technical Report, AEA Technology.

Duderstadt, J.J., Martin, W.R., 1979. Transport Theory. Wiley-Interscience.

Gubbins, M.E., Roth, M.J., 1980. The WIMS-E module W-COND. Technical Report AEEW-M–1772, UKAEA Atomic Energy Establishment, Winfrith.

Hébert, A., 2020. Applied Reactor Physics. Presses Internationales Polytechnique.

Honeck, H.C., 1964. The calculation of the thermal utilization and disadvantage factor in uranium/water lattices. Nucl. Sci. Eng. 18 (1), 49–68.

International Atomic Energy Agency, 2014. Criticality Safety in the Handling of Fissile Material. In: Number SSG-27 in Specific Safety Guides, International Atomic Energy Agency, Vienna.

Irish, E.R., Reas, W.H., 1957. The PUREX Process - A Solvent Extraction Reprocessing Method for Irradiated Uranium. Technical Report HW-49483 A, General Electric.

Jonsson, A., 1963. THESEUS - A One Group Collision Probability Routine for Annular Systems. Technical Report AEEW-R253, UKAEA Atomic Energy Establishment, Winfrith.

Kimpland, R.H., 1993. A Multi-Region Computer Model for Predicting Nuclear Excursions in Aqueous Homeogeneous Assemblies (Ph.D. thesis). The University of Arizona.

Knief, R.A., 1985. Nuclear Criticality Safety Theory and Practice. American Nuclear Society, Inc, 555 North Kensington Avenue, La Grange Park, Illinois 60526 U.S.A.

Lee, J.C., 2020. Nuclear Reactor Physics and Engineering. Wiley and Sons.

Lefvert, T., 1979. New applications of the collision probability method in neutron transport theory. Prog. Nucl. Energy 4 (2), 97–118.

Leppänen, J., Pusa, M., Fridman, E., 2016. Overview of methodology for spatial homogenization in the serpent 2 Monte Carlo code. Ann. Nucl. Energy 96, 126–136.

Leppänen, J., Pusa, M., Viitanen, T., Valtavirta, V., Kaltiaisenaho, T., 2015. The Serpent Monte Carlo code: Status, development and applications in 2013. Ann. Nucl. Energy 82, 142–150.

Lindley, B., Hosking, J., Smith, P., Powney, D., Tollit, B., Newton, T., Perry, R., Ware, T., Smith, P., 2017. Current status of the reactor physics code WIMS and recent developments. Ann. Nucl. Energy 102, 148–157.

Lindley, B., Newton, T., Hosking, G., Smith, P., Powney, D., Smith, P., 2015. Release of WIMS10: A versatile reactor physics code for thermal and fast systems. In: International Congress on Advances in Nuclear Power Plants (ICAPP). Nice, France, 3 - 6 May 2015.

McLaughlin, T.P., 2003. Process criticality accident likelihoods, magnitudes and emergency planning - A focus on solution accidents. In: International Conference on Nuclear Criticality Safety. Challenges in the Persuit of Global Nuclear Criticality Safety. Tokai, Ibaraki (Japan), pp. 831–836, 20 - 24 October.

McLaughlin, T.P., Monahan, S.P., Pruvost, N.L., Frolov, V.V., Ryazanov, B.G., Sviridov, V.I., 2000. A Review of Criticality Accidents. Los Alamos National Laboratory.

Mohanakrishnan, P., Singh, O.P., Umasankari, K. (Eds.), 2021. Physics of Nuclear Reactors. Academic Press.

Oka, Y. (Ed.), 2014. Nuclear Reactor Design. Springer.

Ornstein, L., Uhlenbeck, G., 1937. Some kinetic problems regarding the motion of neutrons through paraffine. Physica 4 (6), 478–486.

Peierls, R., 1939. Critical conditions in neutron multiplication. Math. Proc. Camb. Phil. Soc. 35 (4), 610–615.

Petkov, P.T., Takeda, T., 1998. Transport calculations of MOX and UO_2 pin cells by the method of characteristics. J. Nucl. Sci. Technol. 35 (12), 874–885.

Powney, D.J., Newton, T.D., 2004. Overview of The WIMS 9 Resonance Treatment: A Report Produced for ANSWERS. Technical Report ANSWERS/WIMS/TR.26, Serco Assurance.

Roth, M.J., 1974. Resonance Absorption in Complicated Geometries. Technical Report AEEW-R 921, United Kingdom Atomic Energy Establishment, Winfrith.

Roth, M.J., 1980. The WIMS-E module W-HEAD. Technical Report AEEW-R–1322, UKAEA Atomic Energy Establishment, Winfrith.

Roth, M.J., 1983. The WIMS-E modules W-PRES and W-RES. Technical Report AEEW-R–1707, UKAEA Atomic Energy Establishment, Winfrith.

Roth, M.J., 1985. The Collision Probability Modules of WIMS-E. Technical Report AEEW-R–1920, UKAEA Atomic Energy Establishment, Winfrith.

Srinivasan, M., Rao, K.S., Chandramoleshwar, K., 1992. A TCF approach to the criticality aspects of fissile solution systems. Ann. Nucl. Energy 19, 473–476.

Stacey, W.M., 2007. Nuclear Reactor Phsyics. Wiley-VCH.

Ushio, T., Takeda, T., Mori, M., 2003. Neutron anisotropic scattering effect in heterogeneous cell calculations of light water reactors. J. Nucl. Sci. Technol. 40 (7), 464–480.

Vladimirov, V.S., 1963. Mathematical Problems in the One-Velocity Theory of Particle Transport. Technical Report AECL–1661.

Werner, C.J., Bull, J.S., Solomon, C.J., Brown, F.B., McKinney, G.W., Rising, M.E., Dixon, D.A., Martz, R.L., Hughes, H.G., Cox, L.J., Zukaitis, A.J., Armstrong, J.C., Forster, R.A., Casswell, L., 2018. MCNP Version 6.2 Release Notes. Technical Report LA-UR-18-20808, Los Alamos National Laboratory.

Williams, M.M.R., 1971. Mathematical Methods in Particle Transport Theory. Wiley-Interscience.

Wilson, P.D. (Ed.), 1996. The Nuclear Fuel Cycle: From Ore to Waste. Oxford University Press.

Yamamoto, A., Kitamura, Y., Yamane, Y., 2008. Simplified treatments of anisotropic scattering in LWR core calculations. J. Nucl. Sci. Technol. 45 (3), 217–229.

Zohuri, B., 2016. Neutronic Analysis for Nuclear Reactor Systems. Springer International Publishing.